WILEY

A series of Duffy-distance transformation for integrating 2D and 3D vertex singularities

Jia-He Lv[1,2,4] | Yu-Yong Jiao[1] | Xia-Ting Feng[2,3] | Peter Wriggers[4] |
Xiao-Ying Zhuang[4] | Timon Rabczuk[5]

[1]Faculty of Engineering, China University of Geosciences, Wuhan, China

[2]State Key Laboratory of Geomechanics and Geotechnical Engineering, Institute of Rock and Soil Mechanics, Chinese Academy of Sciences, Wuhan, China

[3]Key Laboratory of the Ministry of Education on Safe Mining of Deep Metal Mines, School of Resources and Civil Engineering, Northeastern University, Shenyang, China

[4]Institute of Continuum Mechanics, Leibniz University Hannover, Hannover, Germany

[5]Institute of Structural Mechanics, Bauhaus University Weimar, Weimar, Germany

Correspondence
Yu-Yong Jiao, Faculty of Engineering, China University of Geosciences, Wuhan 430074, China.
Email: yyjiao@cug.edu.cn

Summary

With the development of the generalized/extended finite element method for fracture problems, the accurate and efficient integration of singular enrichment functions has been an open issue, especially for the 3D case. In this paper, we reveal the near singularities caused by distorted integral patch/cell shape numerically and theoretically during the implementation of generalized Duffy transformation, and the Duffy-distance transformation is developed step by step for the 2D and 3D vertex singularities. Meanwhile, the 3D conformal pre-conditioning strategy is constructed to eliminate the near singularity caused by element shape distortion during the iso-parametric transformation, which enables the Duffy-distance transformation to be applicable for arbitrary shaped tetrahedral elements. As a result, the near singularities can be fully or partly canceled depending on the order of singularity. The implementation of the proposed scheme in existing codes is straightforward. Numerous numerical examples for arbitrary shaped triangles and tetrahedrons are presented to demonstrate its robustness and efficiency, along with comparisons to the generalized Duffy transformation.

KEYWORDS

distance transformation, Duffy transformation, near singularity, numerical quadrature, vertex singularity

1 | INTRODUCTION

In standard finite element method (FEM), shape functions are usually based on polynomials, and the Gauss quadrature is widely used to integrate polynomial functions exactly with an appropriate number of evaluation points. However, it is not able to provide fast and accurate integration for fracture problems due to the need to integrate singular functions at the crack tip. The development of the generalized FEM (GFEM)[1,2] and the extended FEM (XFEM)[3-5] presents an elegant and efficient solution to this issue, as well as the numerical manifold method.[6-9] The fundamental idea of these methods is to enrich the approximation space with a priori knowledge of local solution space via the partition of unity method,[10] such as the asymptotic property of displacement field (ie, $u \sim r^{1/2}$) around the crack tip in the linear elastic fracture mechanics

(LEFM). In consequence, the strain-displacement matrix contains the $O(1/\sqrt{r})$ singularity, and therefore, some entries in the element stiffness matrix have $O(1/\sqrt{r})$ and $O(1/r)$ singularities, which are very harmful for the convergence of integrations. Similarly, some other orders of $O(1/r^{\alpha})$ singularities have also been addressed for different situations in literature, such as HRR crack-tip field,[11] hydraulic fracture,[12] and parametric enrichment for singular problems.[13]

Standard Gauss quadrature fails to evaluate these integrals owing to its discontinuity and various orders of singularities. To obtain accurate numerical integration of such integrals, subdivision into conforming subdomains and high order Gauss quadrature is necessary,[4,5] which lead to increase of computational cost. Therefore, numerous efforts have been devoted to this critical problem,[14-31] among which the variable transformation methods seem to be more promising due to their accuracy and straightforward implementation, such as the well-known Duffy transformation[20] and the polar coordinate transformation. The determination of the transformation Jacobian plays the role to cancel or weaken the singularity. Laborde et al[21] triangulate the element with the singular point inside and then applied the Duffy transformation to integrate singular functions for each subdomain. Mousavi and Sukumar[22,23] show that the Duffy transformation is efficient for $O(1/r)$ singularity, but not as efficient for $O(1/r^{\alpha})$ singularity when $\alpha \neq 1$, and then generalize the Duffy transformation to power singularities of the form $O(1/r^{\alpha})$ for triangles and pyramids. Moreno et al[24-26] present a general and systematic framework for singular transformations, with specific treatment of the radial and angular variables for 3D case. Béchet et al[27] utilize an improved polar coordinate by incorporating a parabolic transformation and propose a superposition technique to integrate on elements that are not containing the singularity. Park et al[28] use another varietal polar coordinate mapping proposed by Nagarajan and Mukherjee[29] and generate it into 3D crack problems. Minnebo[30] presents extensions of the existing Duffy and parabolic transformations to integrate singular functions in 3D, taking into account all configurations of singularity location. However, the accurate and efficient integration of singular enrichment functions has still been an open issue in the GFEM/XFEM literature,[31] especially for the 3D case.

Unlike the weak vertex singularity, less attention has been devoted in current literature to the near singularities caused by distorted integral patch/cell shape, which have been well addressed in the boundary element method (BEM).[32-39] In this paper, we reveal the near singularities caused by distorted integral patch/cell shape numerically and theoretically during the implementation of generalized Duffy transformation, and the Duffy-distance transformation is developed step by step for the 2D and 3D vertex singularities. Meanwhile, the 3D conformal preconditioning strategy is constructed to eliminate the near singularity caused by element shape distortion during the iso-parametric transformation, which enables the Duffy-distance transformation to be applicable for arbitrary shaped tetrahedral elements. This paper is organized as follows. The existing widely used variable transformation methods are briefly reviewed and tested in Section 2. The near singularities caused by distorted integral patch/cell shape are discovered in Section 3 and Section 4, respectively, as well as the construction of Duffy-distance transformation. Section 5 gives the extension of 3D Duffy-distance transformation to arbitrary shaped tetrahedrons. The meaningful 3D conformal preconditioning strategy is deduced in Section 6. Each section is accompanied with numerical verifications to demonstrate its robustness and efficiency. The paper ends with summaries and some remarks. For generalization, vertex singularities with $\alpha = 1$ or $1/2$ for LEFM are selected as paradigms. The relative errors are calculated with error $= \frac{|I_{\text{num}} - I_{\text{ref}}|}{I_{\text{ref}}}$, where the subscripts "num" and "ref" refer to the numerical and reference solutions, respectively. Besides, the abbreviations 'DT', 'DDT', and 'CDDT' used in figures denote the generalized Duffy transformation, the Duffy-distance transformation, and the Duffy-distance transformation with conformal preconditioning strategy, respectively.

2 | BASIC MAPPINGS

In this section, the widely used variable transformation methods, such as the Duffy transformation, the parabolic transformation, and the polar coordinate transformation, are briefly reviewed and tested in details with emphasis on the sensitivity to integral patch shape. Besides, both the parabolic transformation and the polar coordinate transformation are extended to a general form applicable for various orders of vertex singularity.

2.1 | Duffy transformation

The well-known Duffy transformation[20] firstly maps an arbitrary triangular patch in space-xy to the standard right-angled triangle in space-$\xi\eta$, with the singular vertex 1 located at the origin (Figure 1A-B), and then, by using the transformation $\xi = u, \ \eta = uv$, the standard triangle is further cast into a unit quadrilateral $[0, 1] \times [0, 1]$, with singular vertex located at
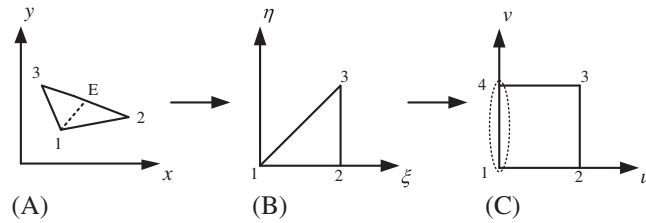
FIGURE 1 Duffy transformation

edge 14 (Figure 1B-C). Easily to confirm that the determinant of Jacobian matrix of Duffy transformation is $|\mathbf{J}_{\text{Duffy}}| = 2Au$, A is the area of triangle $\triangle 123$. Moreover, the square distance from arbitrary point inside $\triangle 123$ to point 1 can be expressed as

$$
\begin{aligned}
r^2 &= \sum_{k=1}^{2} \left(x_k - x_k^{(1)} \right)^2 \\
&= \sum_{k=1}^{2} \left[-\xi x_k^{(1)} + (\xi - \eta) x_k^{(2)} + \eta x_k^{(3)} \right]^2 \\
&= u^2 \sum_{k=1}^{2} \left[(1 - v) x_k^{(2)} + v x_k^{(3)} - x_k^{(1)} \right]^2 \\
&= u^2 \sum_{k=1}^{2} \left(x_k^{(E)} - x_k^{(1)} \right)^2 \\
&= u^2 \mathbf{r}_{1E}^2,
\end{aligned}
\tag{1}
$$

in which the linear interpolation term $(1 - v) x_k^{(2)} + v x_k^{(3)}$ actually represents arbitrary point $\mathbf{x}^{(E)}$ on edge 23, and $\mathbf{r}_{1E}$ denotes the vector from singularity point 1 to point E. Consequently, the Jacobian of Duffy transformation can fully cancel the singularity of type $O(1/r)$. However, for power singularities of the form $O(1/r^\alpha)$, the Duffy transformation behaves poorly due to the appearance of irrational term $u^{1-\alpha}$. Mousavi and Sukumar[22] generalized the Duffy transformation as $\xi = u^\beta$, $\eta = u^\beta v$ to power singularity of the form $f(x,y)/r^\alpha$ with $r = u^\beta |\mathbf{r}_{1E}|$ and $|\mathbf{J}_{\text{Duffy}}| = 2A\beta u^{2\beta - 1}$. The integrals with $O(1/r^\alpha)$ vertex singularity can be expressed as

$$
\iint \frac{f(x,y)}{r^\alpha} dx dy = \iint \frac{f(u,v)}{|\mathbf{r}_{1E}|^\alpha} 2\beta A u^{2\beta-1-\alpha\beta} du dv,
\tag{2}
$$

where $f(x,y)$ is a smooth polynomial function. For $\alpha < 2$, the coefficient β is selected as the minimum integer so that the exponent $2\beta - 1 - \alpha\beta$ is a positive integer. Even though the generalized Duffy transformation seems to be optimal, numerical tests below show that the accuracy is yet very sensitive to the patch shape since the appearance of term $|\mathbf{r}_{1E}|^\alpha$.

Example 2.1 (Sensitivity of generalized Duffy transformation to inclined angle).
To examine the performance of generalized Duffy transformation, taking triangular patches with nodes $(0, 0)$, $(1, 0)$, and $(\cos\theta, \sin\theta)$ as examples, θ is the inclined angle at singular point 1, and the relative errors of generalized Duffy transformation for $1/r^\alpha (\alpha = 1 \text{ or } 1/2)$ are plotted in Figure 2. As it can be easily seen, the accuracy decreases dramatically as θ becomes larger. For integral patches with big obtuse angles proximal to 180°, the distance $|\mathbf{r}_{1E}|$ from singular point to opposite side varies acutely, leading to near singularity in Equation (2).

2.2 | Parabolic transformation

The parabolic transformation utilized by Minnebo[30] can be decomposed into the generalized Duffy transformation with $\beta = 2$ (Figure 3A-C) and a sinh transformation in v-direction (Figure 3C-D) with $v = 0.5(1 + \sinh \tilde{v})$, $\tilde{v} \in [\ln(\sqrt{2} - 1,) \ln(\sqrt{2} + 1)]$, resulting in $\xi = u^2$, $\eta = 0.5u^2(1 + \sinh \tilde{v})$, which is only suitable for $\alpha = 1$ or $1/2$. Additionally, it can be modified into the following general form to accommodate various orders of singularity:

$$
\begin{cases}
\xi = u^\beta \\
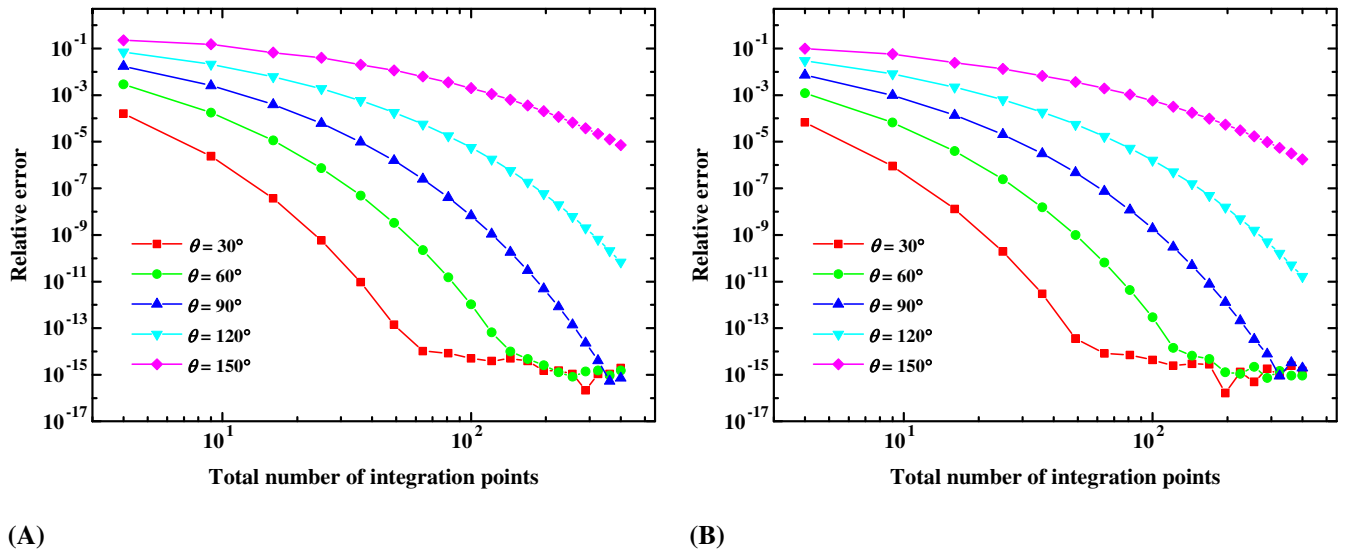\eta = 0.5u^\beta (1 + \sinh \tilde{v}),
\end{cases}
\tag{3}
$$

FIGURE 2 Sensitivity of generalized Duffy transformation to inclined angle. A, $\alpha = 1$; B, $\alpha = 1/2$ [Colour figure can be viewed at wileyonlinelibrary.com]
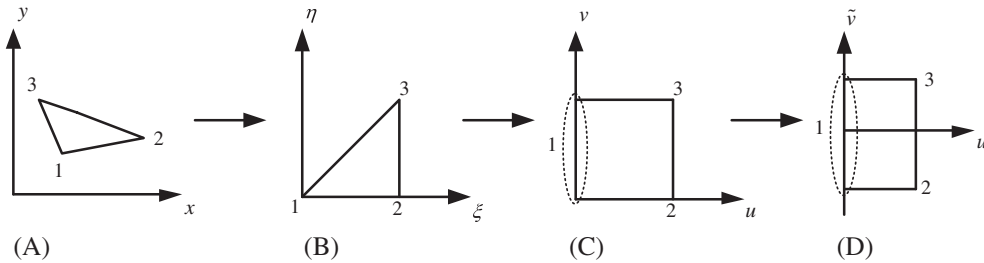

FIGURE 3 Decomposition of parabolic transformation

with $\mid \mathbf{J}_{\text{parab}} \mid = A\beta u^{2\beta-1} \cosh \tilde{v}$, and the integrals with $O(1/r^\alpha)$ vertex singularity can be transformed as

$$\iint \frac{f(x, y)}{r^\alpha} dxdy = \iint \frac{f(u, \tilde{v})}{|\mathbf{r}_{1E}|^\alpha} A\beta u^{2\beta-1-\alpha\beta} \cosh \tilde{v} dud\tilde{v}. \tag{4}$$

Example 2.2 (Sensitivity of parabolic transformation to inclined angle).
To assess the promotion of the v-directional sinh transformation in parabolic transformation, the same triangular patches as 2.1 are tested with $\alpha = 1$ or $1/2$, and the relative errors of parabolic transformation are given in Figure 4. We can observe that the closer θ approaches to 90°, the more accurate results can be obtained compared to the Duffy transformation (see Figure 2), especially, for $\alpha = 1$, 2×2 Gauss points can achieve the machine precision when $\theta = 90°$. Therefore, the appearance of term $\cosh \tilde{v}$ in Equation (4) can partly weaken the near singularity caused by patch shape, which will be proved theoretically in Section 3.

2.3 | Polar coordinate transformation

The conventional polar coordinate transformation establishes a local polar coordinate system with the origin centered at the singular point via $x = \rho \cos \theta$, $y = \rho \sin \theta$, and the singularity of type $O(1/r)$ can be canceled by the Jacobian ρ. Similar to the Duffy transformation, the accuracy is also very sensitive to the patch shape. To overcome this shortcoming, Béchet et al[27] constructed an improved polar coordinate transformation as

$$\begin{cases} \rho = \frac{r_0(1+u)^2}{4\cos\theta} \\ \theta = \sin^{-1}\tanh v, \end{cases} \tag{5}$$
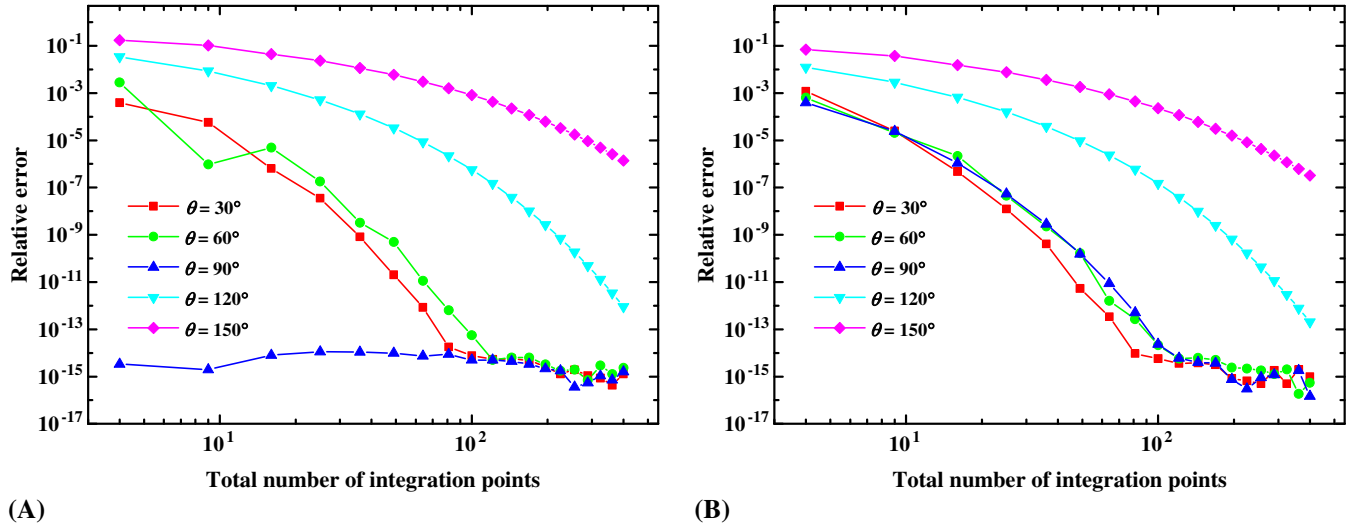
FIGURE 4 Sensitivity of parabolic transformation to inclined angle. A, $\alpha = 1$; B, $\alpha = 1/2$

where r_0 is the orthogonal distance from the opposite side to the singular point, which also gives the reference angle for θ. Equation (5) is suitable for $\alpha = 1$ or $1/2$ and can also be rewritten into a general form as

$$\begin{cases} \rho = \frac{r_0(1+u)^{\beta}}{2^{\beta}\cos\theta} \\ \theta = \sin^{-1}\tanh v, \end{cases} \tag{6}$$

with $dr = \frac{\beta r_0(1+u)^{\beta-1}}{2^{\beta}\cos\theta}du$ and $d\theta = \cos\theta dv$, and the integrals with $O(1/r^{\alpha})$ vertex singularity can be transformed as

$$\iint \frac{f(x,y)}{r^{\alpha}}dxdy = \iint f(\rho,\theta)\rho^{1-\alpha}d\rho d\theta = \iint f(u,v)\frac{\beta r_0^{2-\alpha}(1+u)^{2\beta-1-\alpha\beta}}{2^{(2-\alpha)\beta}\cos^{1-\alpha}\theta}dudv. \tag{7}$$

As we can see, for $\alpha = 1$, the singularity can be totally eliminated, whereas, for $\alpha \neq 1$, the accuracy depends on the term $\cos^{\alpha-1}\theta$.

Example 2.3 (Sensitivity of polar coordinate transformation to inclined angle).
To validate the effectiveness of polar coordinate transformation, the same triangular patches as 2.1 are tested with $\alpha = 1$ or $1/2$, and the relative errors of polar coordinate transformation are presented in Figure 5. As expected, 2×2 Gauss points can always achieve the machine precision for $\alpha = 1$, and for $\alpha = 1/2$, in spite of the sensitivity to patch shape, the polar coordinate transformation delivers higher accuracy compared to the Duffy and parabolic transformations (see Figure 2 and Figure 4).

3 | 2D DUFFY-DISTANCE TRANSFORMATION

In the earlier section, we have discovered the defect of Duffy transformation. Sequentially, the near singularity hidden in patch shape will be revealed theoretically in this section, and also the Duffy-distance transformation will be constructed to damp out the near singularity, along with the Duffy-sinh transformation as a byproduct, which is the general form of previously mentioned parabolic transformation in Section 2.2.

Recalling Equation (1), there exists a one-dimensional linear mapping for edge 23, ie, $x_k^{(E)} = (1-v)x_k^{(2)} + vx_k^{(3)}$, as described in the inset of Figure 6. The following relations can be easily obtained via the Taylor expansion:

$$\begin{aligned} x_k^{(E)} - x_k^{(1)} &= x_k^{(E)} - x_k^{(P)} + x_k^{(P)} - x_k^{(1)} \\ &= \frac{dx_k}{dv}\bigg|_{\mathbf{x}=\mathbf{x}^{(P)}}(v-v_P) + |\mathbf{r}_{1P}|n_k(P), \end{aligned} \tag{8}$$

where point P is the projection point from point 1 to edge 23 with minimum distance $|\mathbf{r}_{1P}|$, v_P is the local coordinate of point P, and $n_k(P)$ represents the components of unit outward normal at point P. If point P is located to the right of point 2
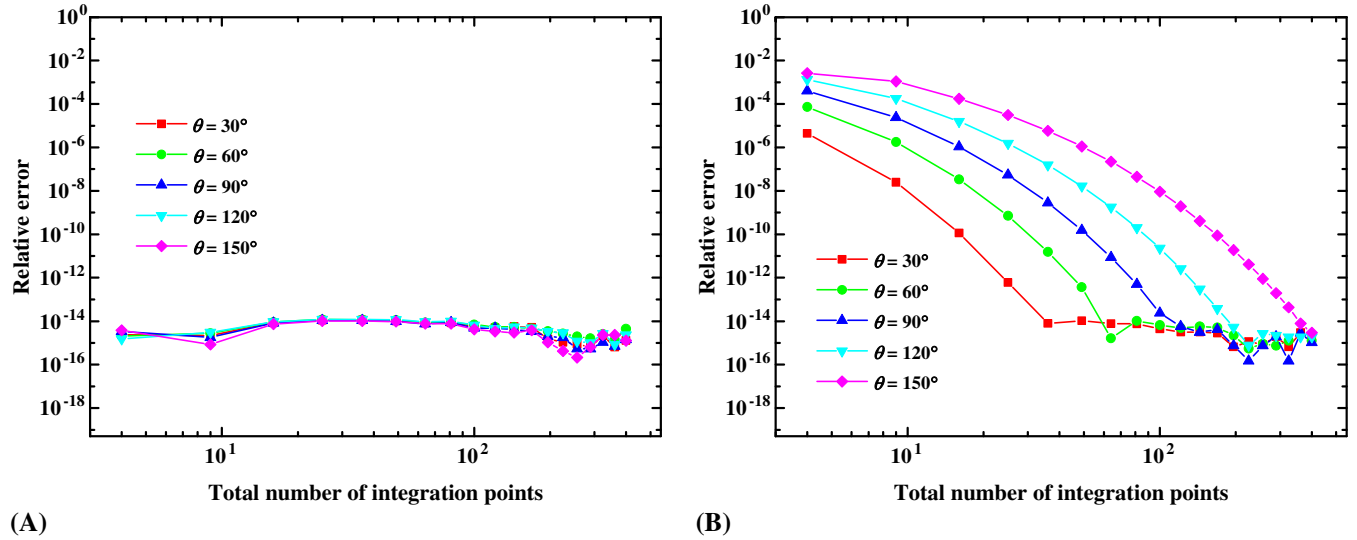
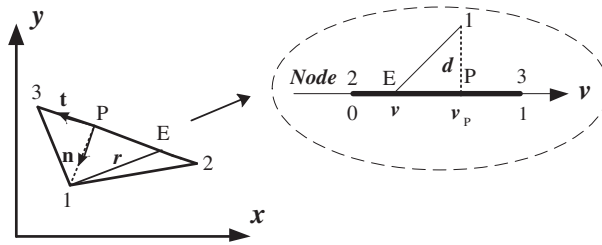**FIGURE 5** Sensitivity of polar coordinate transformation to inclined angle. A, $\alpha = 1$; B, $\alpha = 1/2$

FIGURE 6 Mapping of edge 23 to 1D linear element

in the inset of Figure 6, v_P should be negative, ie, $v_P = -\,|\mathbf{r}_{2P}|\,/\,|\mathbf{r}_{23}|$, otherwise $v_P = |\mathbf{r}_{2P}|\,/\,|\mathbf{r}_{23}|$. Then, the square distance from singularity point 1 to arbitrary point E on edge 23 can be written as

$$
\begin{aligned}
\mathbf{r}_{1E}^2 &= \sum_{k=1}^{2}\left(x_k^{(E)} - x_k^{(1)}\right)^2 \\
&= \sum_{k=1}^{2}\left(\frac{dx_k}{dv}\Big|_{\mathbf{x}=\mathbf{x}^{(P)}}\right)^2 (v - v_P)^2 + \mathbf{r}_{1P}^2 \\
&= J_P^2\left[(v - v_P)^2 + d^2\right].
\end{aligned}
\tag{9}
$$

Note that the Jacobian $J_P = |\mathbf{r}_{23}|$ for straight line, and $d = |\mathbf{r}_{1P}|\,/\,|\mathbf{r}_{23}|$. Taking the triangular patches in 2.1 as example, we give the variation curves of term $1/[(v - v_P)^2 + d^2]$ in Equation (9) as plotted in Figure 7. Obviously, the near singularity with big obtuse inclined angle can be observed.

In order to damp out the near singularity caused by Equation (9), the distance transformation[33,34] in v-direction is introduced as

$$
\begin{cases}
v = \frac{1}{2}\left(e^{\tilde{v}} - d^2 e^{-\tilde{v}}\right) + v_P \\
\tilde{v} = \ln\left[\sqrt{(v - v_P)^2 + d^2} + (v - v_P)\right],
\end{cases}
\tag{10}
$$

with $dv = \sqrt{(v - v_P)^2 + d^2}\,d\tilde{v}$. Plugging Equations (9) and (10) into Equation (2), we have

$$
\begin{aligned}
\iint \frac{f(x, y)}{r^\alpha}dxdy &= \iint \frac{f(u, v)}{|\mathbf{r}_{23}|^\alpha\left[(v - v_P)^2 + d^2\right]^{\alpha/2}}2A\beta u^{2\beta-1-\alpha\beta}dudv \\
&= \iint \frac{f(u, \tilde{v})}{|\mathbf{r}_{23}|^\alpha}2A\beta u^{2\beta-1-\alpha\beta}\left[\left(\frac{e^{\tilde{v}} - d^2 e^{-\tilde{v}}}{2}\right)^2 + d^2\right]^{(1-\alpha)/2}dud\tilde{v}.
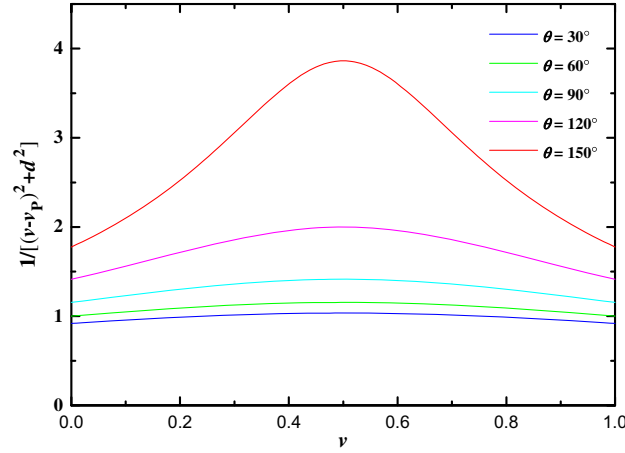\end{aligned}
\tag{11}
$$

FIGURE 7 Variation curves of term $1/[(v - v_P)^2 + d^2]$ for triangular patches in 2.1

We can conclude that, from Equation (11), for $\alpha = 1$, the singularity can be totally eliminated, whereas, for $\alpha \neq 1$, the accuracy still depends on the patch shape slightly.

As an alternative choice, we can also employ the sinh transformation[35,36] in v-direction as

$$
\begin{cases}
v = v_P + d \sinh \tilde{v} \\
\tilde{v} = \operatorname{arc} \sinh \frac{v - v_P}{d},
\end{cases}
\tag{12}
$$

and, correspondingly,

$$
\iint \frac{f(x, y)}{r^\alpha} dxdy = \iint \frac{f(u, v)}{|\mathbf{r}_{23}|^\alpha \left[(v - v_P)^2 + d^2\right]^{\alpha/2}} 2A\beta u^{2\beta - 1 - \alpha\beta} dudv
$$
$$
= \iint \frac{f(u, \tilde{v})}{|\mathbf{r}_{23}|^\alpha} 2A\beta u^{2\beta - 1 - \alpha\beta} d^{(1-\alpha)} \cosh^{(1-\alpha)} \tilde{v} du d\tilde{v}.
\tag{13}
$$

Actually, the parabolic transformation in Section 2.2 can be seen as a special case of the Duffy-sinh transformation with $v_P = 0.5$ and $d = 0.5$. That is why it can achieve machine precision with 2×2 Gauss points only for $\theta = 90°$ in Figure 4A. Numerical tests show that the Duffy-distance and Duffy-sinh transformations can get almost the same results (see Figure 8 and Figure 9).
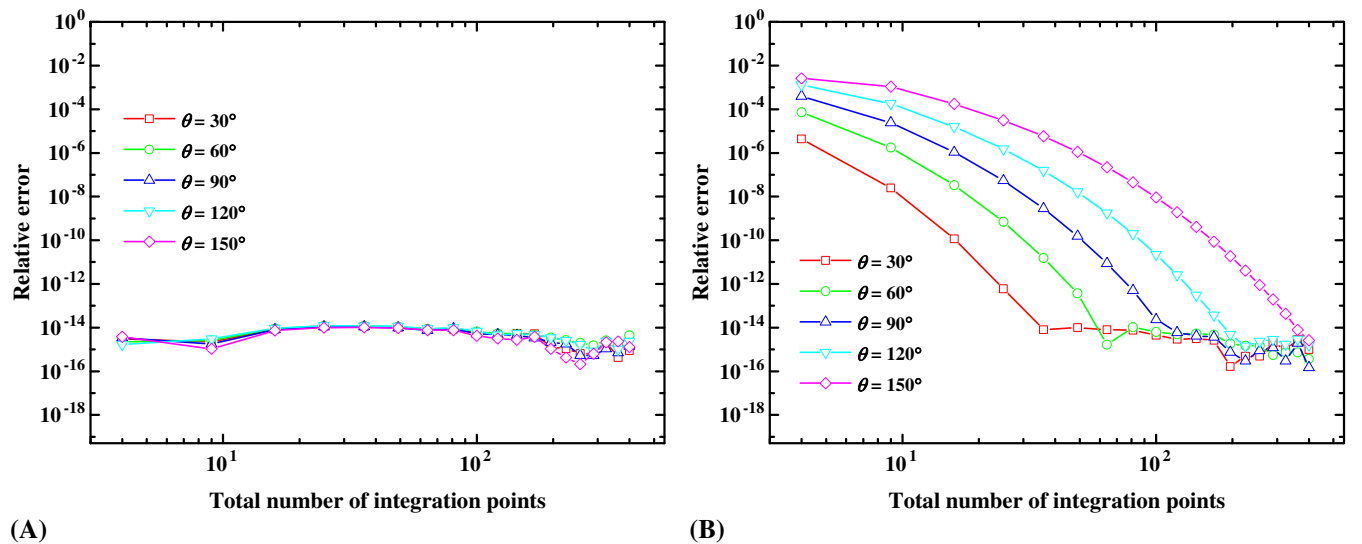

(A)

(B)

FIGURE 8 Sensitivity of Duffy-distance transformation to inclined angle. A, $\alpha = 1$; B, $\alpha = 1/2$
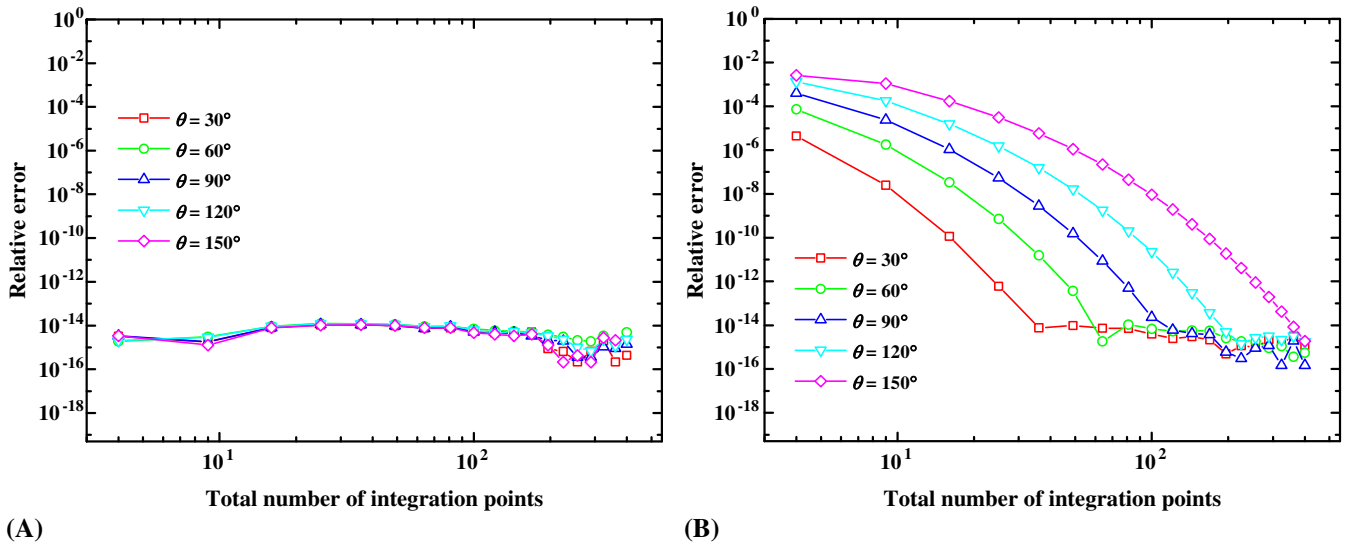
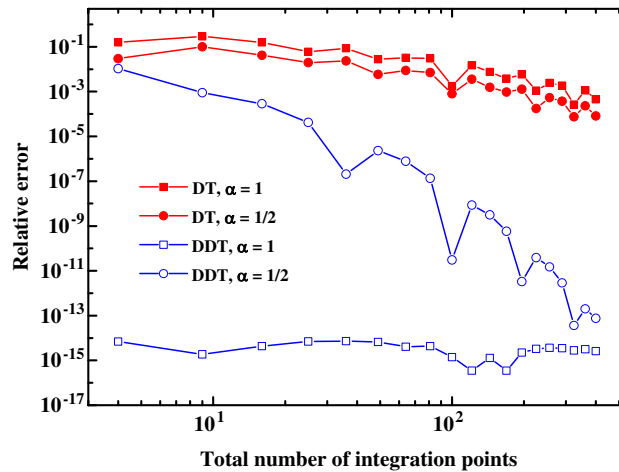**FIGURE 9** Sensitivity of Duffy-sinh transformation to inclined angle. A, $\alpha = 1$; B, $\alpha = 1/2$

FIGURE 10 Comparisons of generalized Duffy and Duffy-distance transformations [Colour figure can be viewed at wileyonlinelibrary.com]

Example 3.1 (Comparisons of generalized Duffy and Duffy-distance transformations)**.**
To verify the effectiveness of Duffy-distance transformation, the same triangular patches as 2.1 are tested with $\alpha = 1$ or $1/2$, and the relative errors for both the Duffy-distance and Duffy-sinh transformations are presented in Figure 8 and Figure 9. It can be easily seen that 2×2 Gauss points can always achieve the machine precision for $\alpha = 1$, and for $\alpha = 1/2$, more accurate results can be obtained compared to the generalized Duffy transformation (see Figure 2), which are almost consistent with the improved polar coordinate transformation (see Figure 5). Moreover, an extremely distorted triangular patch with nodes $(0, 0)$, $(1, 0)$ and $(0.1 \cos 150°,\ 0.1 \sin 150°)$ is concerned, and the superiority of Duffy-distance transformation can be observed obviously in Figure 10.

4 | 3D DUFFY-DISTANCE TRANSFORMATION

In this section, the generalized Duffy transformation is extended to 3D tetrahedral cells, as well as its sensitivity to the shape of tetrahedrons, including the cell height and base triangle shape. In order to circumvent these defects, the 3D Duffy-distance transformation is formulated step by step in details, along with numerous numerical verifications.

4.1 | 3D Duffy transformation

Considering an arbitrary 3D tetrahedron, as shown in Figure 11, the singular vertex lies at point 1, and the base triangle $\Delta 234$ is set to be anticlockwise from the opposite view of singular point. Firstly, mapping the tetrahedron in space-xyz into space-$\xi\eta\zeta$ via the iso-parametric transformation with the singular point located at the origin, and then the extension of Duffy transformation can be implemented using $\xi = u^\beta$, $\eta = u^\beta v$, $\zeta = u^\beta vw$ with $|\mathbf{J}_{\text{Duffy}}| = 6V_{\text{tet}}\beta u^{3\beta-1}v$, V_{tet} denotes the signed volume of tetrahedron. Moreover, the square distance from arbitrary point inside the tetrahedron to singular point 1 can be expressed as

$$
\begin{aligned}
r^2 &= \sum_{k=1}^{3} \left(x_k - x_k^{(1)} \right)^2 \\
&= \sum_{k=1}^{3} \left[-\xi x_k^{(1)} + (\xi - \eta) x_k^{(2)} + (\eta - \zeta) x_k^{(3)} + \zeta x_k^{(4)} \right]^2 \\
&= u^{2\beta} \sum_{k=1}^{3} \left[(1-v) x_k^{(2)} + (v - vw) x_k^{(3)} + vw x_k^{(4)} - x_k^{(1)} \right]^2 \\
&= u^{2\beta} \sum_{k=1}^{3} \left(x_k^{(T)} - x_k^{(1)} \right)^2 \\
&= u^{2\beta} \mathbf{r}_{1T}^2.
\end{aligned}
\tag{14}
$$

We should remark that based on the mapping $\eta = v$ and $\zeta = vw$, the interpolation term $(1-v) x_k^{(2)} + (v-vw) x_k^{(3)} + vw x_k^{(4)}$ actually represents arbitrary point $\mathbf{x}^{(T)}$ on base triangle $\Delta 234$, and $\mathbf{r}_{1T}$ denotes the vector from singular point 1 to point T. In consequence, the integrals with $O(1/r^\alpha)$ vertex singularity can be transformed as

$$
\iiint \frac{f(x,y,z)}{r^\alpha} dx dy dz = \iiint \frac{f(u,v,w)}{\mathbf{r}_{1T}^\alpha} 6\beta V_{\text{tet}} u^{3\beta-1-\alpha\beta} v \, du \, dv \, dw.
\tag{15}
$$

For $\alpha < 3$, the coefficient β is selected as the minimum integer to ensure that the exponent $3\beta - 1 - \alpha\beta$ is a positive integer. Similar to the 2D case, the 3D Duffy transformation will also be sensitive to the shape of tetrahedron due to the appearance of term $|\mathbf{r}_{1T}|$. In order to discover the influence factors of tetrahedron shape, a simple decomposition of $\mathbf{r}_{1T}^2 = \mathbf{r}_{1P}^2 + \mathbf{r}_{PT}^2$ is introduced, where point P denotes the projection point from point 1 to base triangle $\Delta 234$ with minimum distance $|\mathbf{r}_{1P}|$, and the value of $|\mathbf{r}_{PT}|$ depends directly on the shape of base triangle. Therefore, these two aspects will be investigated in details, and for convenience and simplicity, tetrahedrons satisfying the condition of $\mathbf{r}_{12} \perp \Delta 234$ are chosen as examples.

Example 4.1 (Sensitivity of 3D Duffy transformation to cell height).
To demonstrate the influence of cell height, tetrahedrons with nodes $(0,0,h)$, $(0,0,0)$, $(0,1,0)$, and $(1,1,0)$ are taken as examples. The cell height h varies as 1.0, 0.5, 0.2, 0.1, and 0.05, and the relative errors of Duffy transformation for $1/r^\alpha (\alpha = 1 \text{ or } 1/2)$ are presented in Figure 12. As it can be seen, the accuracy drops sharply as h becomes smaller, which is evident to illustrate the influence of cell height.
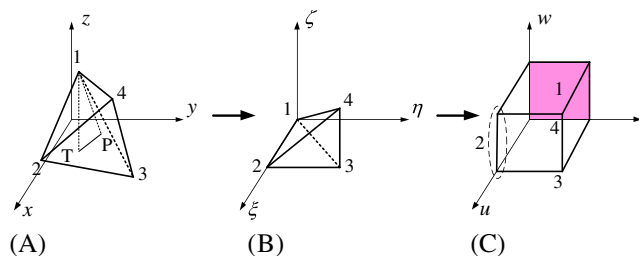

FIGURE 11   3D Duffy transformation [Colour figure can be viewed at wileyonlinelibrary.com]
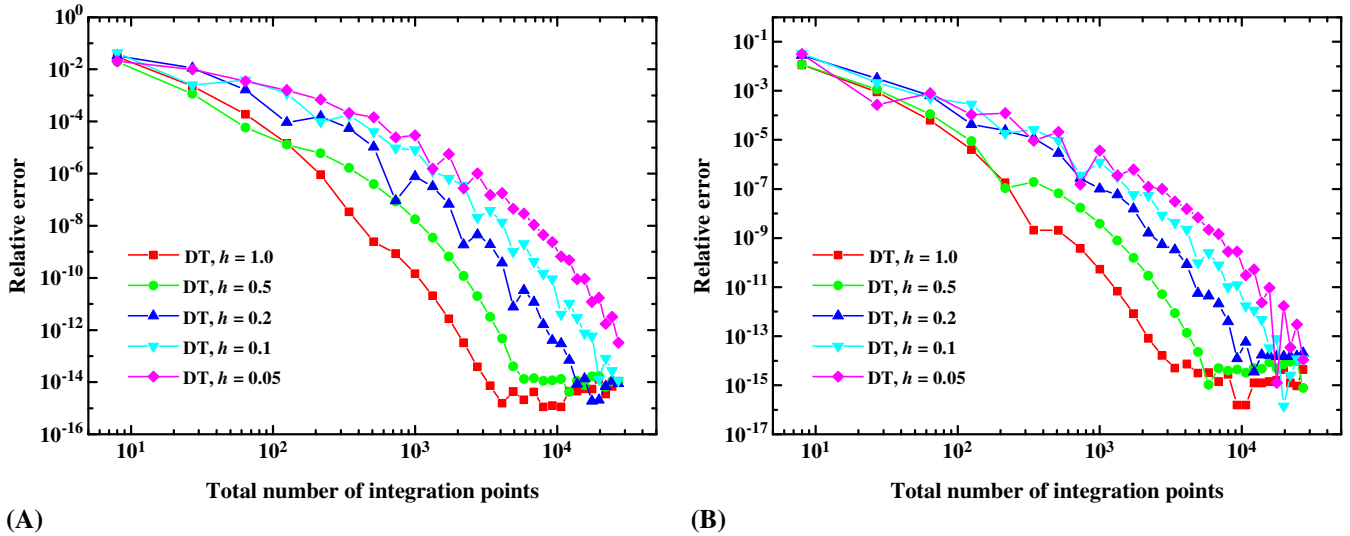
FIGURE 12 Sensitivity of 3D Duffy transformation to cell height. A, $\alpha = 1$; B, $\alpha = 1/2$

4.2 | Near singularity hidden in cell height

To uncover the source of shape influence theoretically, firstly, the tetrahedron satisfying the condition of $\mathbf{r}_{12} \perp \Delta 234$ is mapped into a triangular prism using $\xi = u^\beta$, $\eta = u^\beta v$, $\zeta = u^\beta w$, as shown in Figure 13. Then, a local polar coordinate system centered at projection point $\mathbf{x}^{(2)}$ is established at plane $u = 1$, ie, $v = \rho \cos\theta, w = \rho \sin\theta$ with $\theta \in \left[0, \frac{\pi}{4}\right], \rho \in \left[0, \frac{1}{\cos\theta}\right]$. The following relations can be obtained via the Taylor expansion:

$$
\begin{aligned}
x_k^{(T)} - x_k^{(2)} &= \frac{\partial x_k}{\partial v}\bigg|_{\mathbf{x}=\mathbf{x}^{(2)}} v + \frac{\partial x_k}{\partial w}\bigg|_{\mathbf{x}=\mathbf{x}^{(2)}} w \\
&= \rho \left(\frac{\partial x_k}{\partial v}\bigg|_{\mathbf{x}=\mathbf{x}^{(2)}} \cos\theta + \frac{\partial x_k}{\partial w}\bigg|_{\mathbf{x}=\mathbf{x}^{(2)}} \sin\theta \right),
\end{aligned}
\tag{16}
$$

in which the partial derivative terms can be calculated using the chain rule. In addition, the square distance from arbitrary point $\mathbf{x}^{(T)}$ inside base triangle $\Delta 234$ to projection point 2 can be written as

$$
\begin{aligned}
\mathbf{r}_{2T}^2 &= \sum_{k=1}^{3} \left(x_k^{(T)} - x_k^{(2)} \right)^2 \\
&= \rho^2 \sum_{k=1}^{3} \left(\frac{\partial x_k}{dv}\bigg|_{\mathbf{x}=\mathbf{x}^{(2)}} \cos\theta + \frac{\partial x_k}{dw}\bigg|_{\mathbf{x}=\mathbf{x}^{(2)}} \sin\theta \right)^2 \\
&= \rho^2 A^2(\theta)
\end{aligned}
\tag{17}
$$

with

$$
A(\theta) = \sqrt{\sum_{k=1}^{3} \left(\frac{\partial x_k}{\partial v}\bigg|_{\mathbf{x}=\mathbf{x}^{(2)}} \cos\theta + \frac{\partial x_k}{\partial w}\bigg|_{\mathbf{x}=\mathbf{x}^{(2)}} \sin\theta \right)^2}.
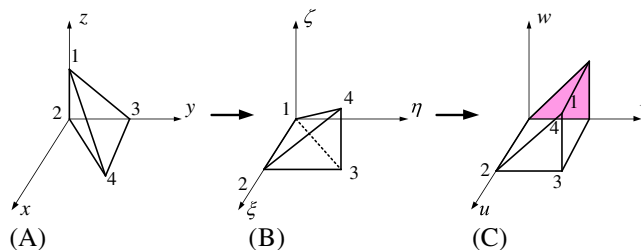\tag{18}
$$

FIGURE 13 3D Duffy-distance transformation [Colour figure can be viewed at wileyonlinelibrary.com]

Finally, the square distance from arbitrary point $\mathbf{x}^{(T)}$ inside base triangle $\Delta 234$ to singular point 1 can be rewritten as

$$
\begin{aligned}
\mathbf{r}_{1T}^2 &= \mathbf{r}_{12}^2 + \mathbf{r}_{2T}^2 \\
&= \mathbf{r}_{12}^2 + \rho^2 A^2(\theta) \\
&= A^2(\theta)\left(\rho^2 + d^2\right),
\end{aligned}
\tag{19}
$$

where $d = |\mathbf{r}_{12}| / A(\theta)$ can be regarded as the characteristic height of tetrahedrons for vertex singularity problem. From Equation (19), we can clearly see the near singularity caused by d, which is related to the cell height of tetrahedrons and $A(\theta)$.

To damp out the near singularity, we introduce the following distance transformation[33,34] used in BEM:

$$
\begin{cases}
\rho(\tilde{\rho}, \theta) = \sqrt{e^{2\tilde{\rho}} - d^2} \\
\tilde{\rho}(\rho, \theta) = \frac{1}{2}\log\left(\rho^2 + d^2\right),
\end{cases}
\tag{20}
$$

with $d\rho = \frac{\rho^2 + d^2}{\rho}d\tilde{\rho} = \frac{e^{2\tilde{\rho}}}{\rho}d\tilde{\rho}$, and correspondingly, Equation (15) can be changed as

$$
\begin{aligned}
\iiint \frac{f(x,y,z)}{r^\alpha}dxdydz &= \iiint \frac{f(u,v,w)}{\mathbf{r}_{1T}^\alpha}6\beta V_{\text{tet}}u^{3\beta-1-\alpha\beta}dudvdw \\
&= \iiint \frac{f(u,\rho,\theta)}{A^\alpha(\theta)}\frac{\rho}{\left(\rho^2+d^2\right)^{\alpha/2}}6V_{\text{tet}}\beta u^{3\beta-1-\alpha\beta}dud\rho d\theta \\
&= \iiint \frac{f(u,\tilde{\rho},\theta)}{A^\alpha(\theta)}6V_{\text{tet}}\beta u^{3\beta-1-\alpha\beta}e^{(2-\alpha)\tilde{\rho}}dud\tilde{\rho}d\theta.
\end{aligned}
\tag{21}
$$

From Equation (21), we can conclude that, for $\alpha = 2$, the near singularity caused by characteristic height can be fully eliminated, whereas, for $\alpha \neq 2$, exponential precision can be expected. It is worth to note that the distance transformation in radial direction can be also replaced by $\rho(\tilde{\rho}, \theta) = \sqrt{\tilde{\rho}^2 - d^2}$ for $\alpha = 1$ with $d\rho = \frac{\sqrt{\rho^2+d^2}}{\rho}d\tilde{\rho}$ and $\rho(\tilde{\rho}, \theta) = \sqrt{\left(\frac{3}{2}\tilde{\rho}\right)^{\frac{4}{3}} - d^2}$ for $\alpha = 1/2$ with $d\rho = \frac{\sqrt[4]{\rho^2+d^2}}{\rho}d\tilde{\rho}$, which will be more accurate. Here, this version of Duffy-distance transformation is named as 3D initial Duffy-distance transformation because the near singularity caused by distorted base shape has not been taken into account, which is denoted as "DDT0" in figures.

Example 4.2 (Sensitivity of 3D initial Duffy-distance transformation to cell height).
To validate the effect of distance transformation, tetrahedrons in 4.1 are tested for $1/r^\alpha(\alpha = 1$ or $1/2)$, and the relative errors of 3D initial Duffy-distance transformation are presented in Figure 14. For convergence of comparisons, the results of 3D Duffy transformation as $h = 1.0$, which is the most accurate case in Figure 12, are remained. It can be
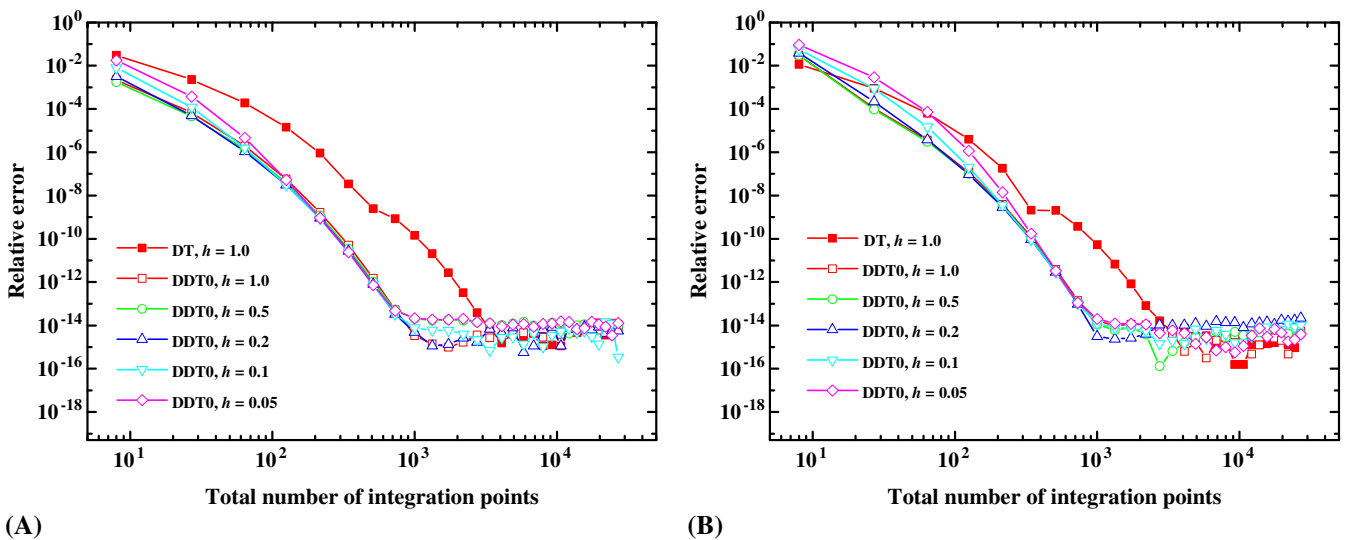

FIGURE 14 Sensitivity of 3D initial Duffy-distance transformation to cell height. A, $\alpha = 1$; B, $\alpha = 1/2$

easily seen that the 3D initial Duffy-distance transformation tends to be more accurate with higher convergence rate for all values of h.

Example 4.3 (Sensitivity of 3D initial Duffy-distance transformation to base triangle shape).

To reveal the influence of base triangle shape, both the inclined angle and the aspect ratio at point 3 are concerned, respectively. Firstly, taking tetrahedrons with nodes $(0, 0, 0.1)$, $(0, 0, 0)$, $(0, 1, 0)$, and $(\sin\theta, 1 - \cos\theta, 0)$ as examples, θ is the inclined angle at point 3, the relative errors of 3D initial Duffy-distance transformation for $1/r^\alpha (\alpha = 1$ or $1/2)$ are presented in Figure 15. We can observe that the accuracy decreases obviously as θ tends to be a sharp angle. Then, tetrahedrons with nodes $(0, 0, 0.1)$, $(0, 0, 0)$, $(0, 1, 0)$, and $(a, 1, 0)$ are tested, the aspect ratio varies from 1.0 to 10.0, the relative errors of 3D initial Duffy-distance transformation are plotted in Figure 16. Obviously, the accuracy drops dramatically with the increase of a.
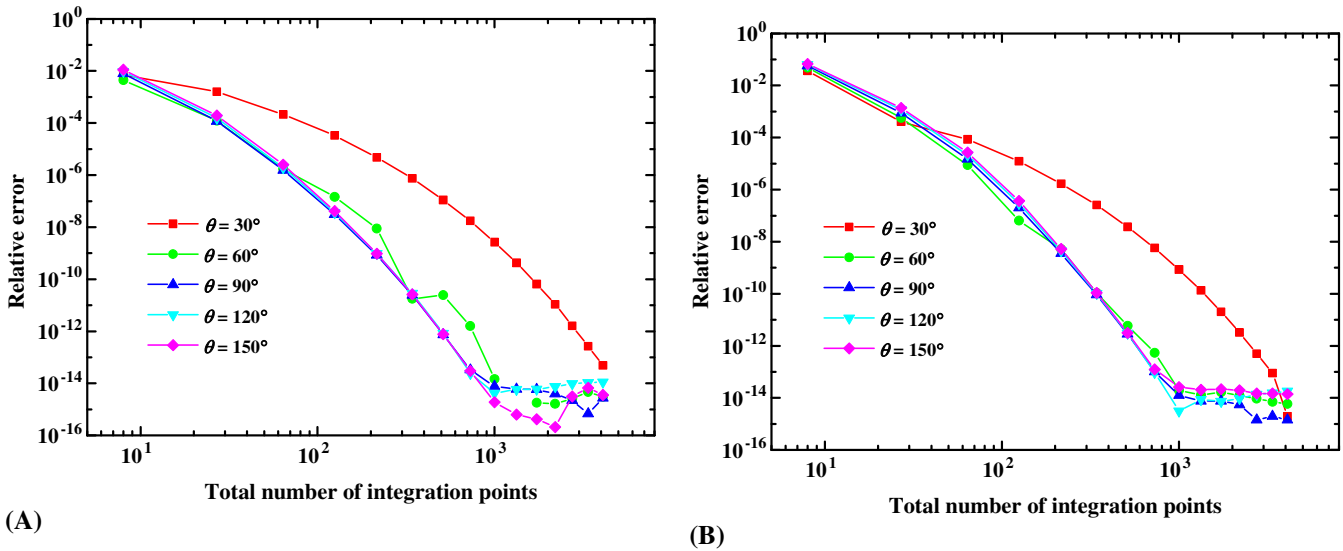

FIGURE 15　Sensitivity of 3D initial Duffy-distance transformation to inclined angle of base triangle. A, $\alpha = 1$; B, $\alpha = 1/2$
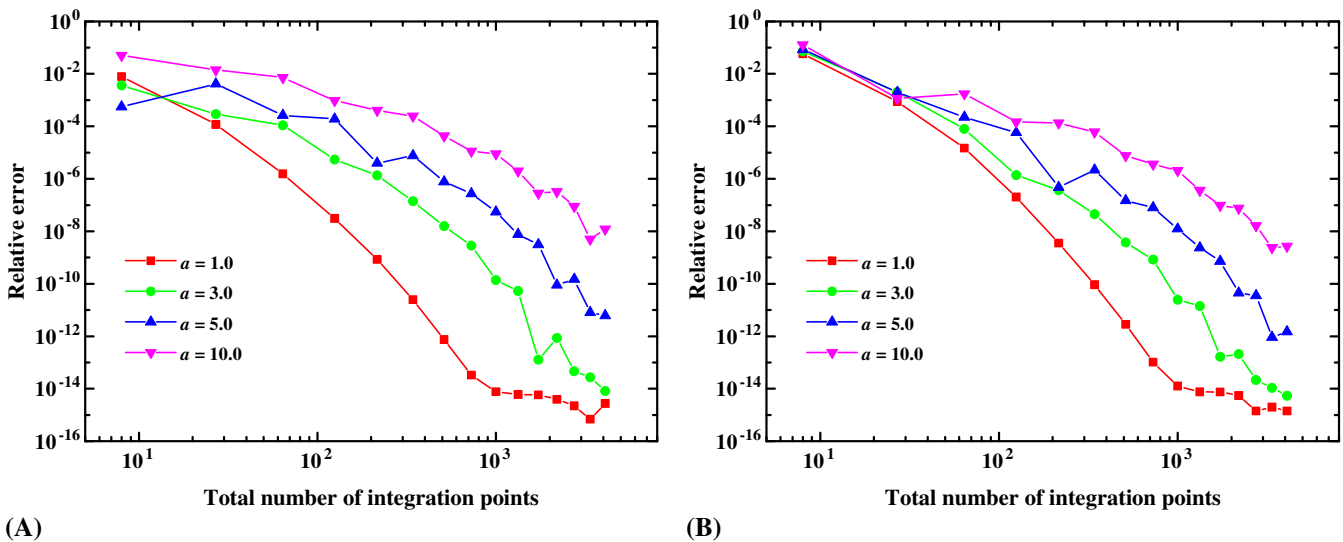

FIGURE 16　Sensitivity of 3D initial Duffy-distance transformation to aspect ratio of base triangle. A, $\alpha = 1$; B, $\alpha = 1/2$ [Colour figure can be viewed at wileyonlinelibrary.com]

4.3 | Near singularity hidden in base triangle shape

Recalling Equation (21), the term $A(\theta)$ is directly related to the base triangle shape, we assume $\mathbf{u}_1$ and $\mathbf{u}_2$ being the two line vectors of Jacobian matrix at projection point $\mathbf{x}^{(2)}$, ie,

$$\mathbf{u}_1 = \left[\frac{\partial x}{\partial v}\Big|_{\mathbf{x}=\mathbf{x}^{(2)}}, \frac{\partial y}{\partial v}\Big|_{\mathbf{x}=\mathbf{x}^{(2)}}, \frac{\partial z}{\partial v}\Big|_{\mathbf{x}=\mathbf{x}^{(2)}}\right] \tag{22}$$

$$\mathbf{u}_2 = \left[\frac{\partial x}{\partial w}\Big|_{\mathbf{x}=\mathbf{x}^{(2)}}, \frac{\partial y}{\partial w}\Big|_{\mathbf{x}=\mathbf{x}^{(2)}}, \frac{\partial z}{\partial w}\Big|_{\mathbf{x}=\mathbf{x}^{(2)}}\right]. \tag{23}$$

Then, Equation (18) can be rewritten as

$$
\begin{aligned}
A(\theta) &= \sqrt{\sum_{k=1}^{3}\left(\frac{\partial x_k}{\partial v}\Big|_{\mathbf{x}=\mathbf{x}^{(2)}}\cos\theta + \frac{\partial x_k}{\partial w}\Big|_{\mathbf{x}=\mathbf{x}^{(2)}}\sin\theta\right)^2}\\
&= \sqrt{\mathbf{u}_1^2\cos^2\theta + \mathbf{u}_2^2\sin^2\theta + \mathbf{u}_1\cdot\mathbf{u}_2\sin 2\theta}\\
&= \sqrt{\frac{1}{2}\left(\mathbf{u}_1^2 + \mathbf{u}_2^2\right) + \frac{1}{2}\left(\mathbf{u}_1^2 - \mathbf{u}_2^2\right)\cos 2\theta + \mathbf{u}_1\cdot\mathbf{u}_2\sin 2\theta}\\
&= \sqrt{\frac{1}{2}\left(\mathbf{u}_1^2 + \mathbf{u}_2^2\right)\left[1 + \mu\sin(2\theta + \varphi)\right]}
\end{aligned}
\tag{24}
$$

with

$$\lambda = \frac{|\mathbf{u}_1|}{|\mathbf{u}_2|}, \quad \cos\gamma = \frac{\mathbf{u}_1\cdot\mathbf{u}_2}{|\mathbf{u}_1||\mathbf{u}_2|} \tag{25}$$

$$\varphi = \arctan\frac{\lambda^2 - 1}{2\lambda\cos\gamma}, \quad \mu = \sqrt{1 - \frac{4\sin^2\gamma}{(\lambda + \lambda^{-1})^2}}. \tag{26}$$

Actually, $\mathbf{u}_1 = \mathbf{r}_{23} = [x_3 - x_2, y_3 - y_2, z_3 - z_2]$ and $\mathbf{u}_2 = \mathbf{r}_{34} = [x_4 - x_3, y_4 - y_3, z_4 - z_3]$, hence λ and γ represent the aspect ratio and the supplementary angle of the inclined angle at point 3, rather than point 2. We can conclude that, from Equations (24)-(26), for base triangles with distorted shape, such as large aspect ratio, peak angle or large obtuse angle at point 3, $\mu \to 1$, if $\sin(2\theta + \varphi) \to -1$ simultaneously, $A(\theta) \to 0$, resulting in another near singularity.[38,39] That is why the precision decreases in example 4.3.

It is worthy to note that, if

$$|\mathbf{u}_1| = |\mathbf{u}_2|, \quad \mathbf{u}_1 \bullet \mathbf{u}_2 = 0. \tag{27}$$

$A(\theta)$ in Equation (24) will be a constant, $A(\theta) = |\mathbf{u}_1| = |\mathbf{u}_2|$. In order to satisfy the aforementioned conditions, a conformal preconditioning strategy[38,39] is developed to eliminate the near singularity caused by distorted base triangle shape.

Considering an arbitrary base triangle as shown in Figure 17, firstly, the triangle in space-xyz is mapped into a right-angled unit triangle in space-vw by the iso-parametric transformation, and then the unit triangle is further cast into a new triangle in space-$\tilde{v}\tilde{w}$ by the inverse interpolation

$$\tilde{\mathbf{x}} = \sum_{i=2}^{4}\phi_i(v, w)\tilde{\mathbf{x}}^{(i)} \tag{28}$$
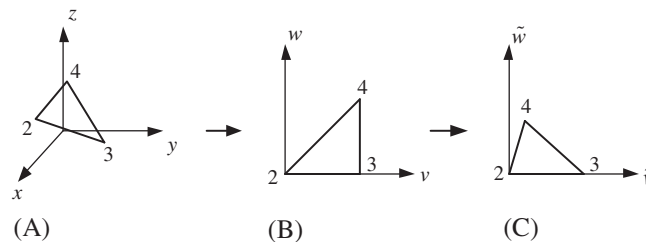

FIGURE 17 Conformal preconditioning strategy for base triangle

with

$$\phi_2(v, w) = 1 - v, \quad \phi_3(v, w) = v - w, \quad \phi_4(v, w) = w, \tag{29}$$

where $\tilde{\mathbf{x}}^{(i)}$ is the node coordinates of new triangle. Plugging Equation (29) into Equation (28) yields

$$\begin{bmatrix} \tilde{v} \\ \tilde{w} \end{bmatrix} = \mathbf{T} \begin{bmatrix} 1 \\ v \\ w \end{bmatrix}, \quad \mathbf{T} = \begin{bmatrix} \tilde{v}^{(2)} & \tilde{v}^{(3)} - \tilde{v}^{(2)} & \tilde{v}^{(4)} - \tilde{v}^{(3)} \\ \tilde{w}^{(2)} & \tilde{w}^{(3)} - \tilde{w}^{(2)} & \tilde{w}^{(4)} - \tilde{w}^{(3)} \end{bmatrix}. \tag{30}$$

To obtain a linear mapping from space-vw to space-$\tilde{v}\tilde{w}$, $(\tilde{v}^{(2)}, \tilde{w}^{(2)})$ is set to be $(0, 0)$. Note that only two equations can be constructed in Equation (27), here, we can assume $(\tilde{v}^{(3)}, \tilde{w}^{(3)}) = (1, 0)$(or another case with $(\tilde{v}^{(4)}, \tilde{w}^{(4)}) = (0, 1)$), and the transformation matrix $\mathbf{T}$ can be rewritten as

$$\mathbf{T} = \begin{bmatrix} 1 & \tilde{v}^{(4)} - 1 \\ 0 & \tilde{w}^{(4)} \end{bmatrix}, \quad \mathbf{T}^{-1} = \frac{1}{|\mathbf{T}|} \begin{bmatrix} \tilde{w}^{(4)} & 1 - \tilde{v}^{(4)} \\ 0 & 1 \end{bmatrix}. \tag{31}$$

Correspondingly, the two line vectors of Jacobian matrix at projection point $\tilde{\mathbf{x}}^{(2)}$ in space space-$\tilde{v}\tilde{w}$ can be further transformed as

$$(\tilde{\mathbf{u}}_1, \tilde{\mathbf{u}}_2) = (\mathbf{u}_1, \mathbf{u}_2) \mathbf{T}^{-1} = \frac{1}{|\mathbf{T}|} \left[\tilde{w}^{(4)} \mathbf{u}_1 \left(1 - \tilde{v}^{(4)}\right) \mathbf{u}_1 + \mathbf{u}_2 \right]. \tag{32}$$

Solving Equation (27) with $\tilde{\mathbf{u}}_1$ and $\tilde{\mathbf{u}}_2$, we have $(\tilde{v}^{(4)}, \tilde{w}^{(4)}) = (\frac{\lambda + \cos\gamma}{\lambda}, \pm\frac{\sin\gamma}{\lambda})$. For the case $\tilde{w}^{(4)} = -\frac{\sin\gamma}{\lambda}$, the area of triangle $\Delta 234$ in space-$\tilde{v}\tilde{w}$ is negative, in other words, the new triangle is clockwise. Therefore, $\tilde{w}^{(4)} = \frac{\sin\gamma}{\lambda}$ is selected as the final solution with

$$\mathbf{T} = \begin{bmatrix} 1 & \frac{\cos\gamma}{\lambda} \\ 0 & \frac{\sin\gamma}{\lambda} \end{bmatrix}, \quad \mathbf{T}^{-1} = \begin{bmatrix} 1 & -\frac{\cos\gamma}{\sin\gamma} \\ 0 & \frac{\lambda}{\sin\gamma} \end{bmatrix}. \tag{33}$$

After applying the conformal preconditioning strategy, a constant $A(\theta)$ can be obtained. Then, the local polar coordinate system is established in transformed space-$\tilde{v}\tilde{w}$ with $\tilde{v} = \rho\cos\theta$ and $\tilde{w} = \rho\sin\theta$, and Equation (21) can be rewritten as

$$\begin{aligned}
\iiint \frac{f(x, y, z)}{r^\alpha} dx dy dz &= \iiint \frac{f(u, v, w)}{\mathbf{r}_{1T}^\alpha} 6\beta V_{\text{tet}} u^{3\beta - 1 - \alpha\beta} du dv dw \\
&= \iiint \frac{f(u, \tilde{v}, \tilde{w})}{\mathbf{r}_{1T}^\alpha} 6\beta V_{\text{tet}} u^{3\beta - 1 - \alpha\beta} |\mathbf{T}^{-1}| du d\tilde{v} d\tilde{w} \\
&= \iiint \frac{f(u, \rho, \theta)}{A^\alpha(\theta)} \frac{\rho}{(\rho^2 + d^2)^{\alpha/2}} 6 V_{\text{tet}} \beta u^{3\beta - 1 - \alpha\beta} |\mathbf{T}^{-1}| du d\rho d\theta.
\end{aligned} \tag{34}$$

Note that the conformal preconditioning strategy transforms the right-angled unit triangle in Figure 17B into a new triangle in space-$\tilde{v}\tilde{w}$, which is similar to the original shape. Hence, we should take into account the near singularity caused by distorted patch shape during the polar coordinate transformation (as illustrated in Section 2.3). Before applying the distance transformation, the following mapping is utilized:

$$\rho = \frac{r_0 \bar{\rho}}{\cos\theta}, \tag{35}$$

where r_0 is the orthogonal distance from the opposite side to the singular point, which also gives the reference angle for θ. And correspondingly, Equation (17) can be rewritten as

$$\begin{aligned}
\mathbf{r}_{1T}^2 &= A^2(\theta) \left(\rho^2 + d^2\right) \\
&= A^2(\theta) \left(\frac{r_0^2 \bar{\rho}^2}{\cos^2\theta} + d^2\right) \\
&= A^2(\theta) \frac{r_0^2}{\cos^2\theta} \left(\bar{\rho}^2 + \tilde{d}^2\right),
\end{aligned} \tag{36}$$

with $\tilde{d} = d\cos\theta/r_0$. After plugging the distance transformation $\bar{\rho}(\tilde{\rho}, \theta) = \sqrt{e^{2\tilde{\rho}} - \tilde{d}^2}$, Equation (34) can be rewritten as

$$
\iiint \frac{f(x,y,z)}{r^\alpha} dxdydz = \iiint \frac{f(u,\rho,\theta)}{A^\alpha(\theta)} \frac{\rho}{(\rho^2 + d^2)^{\alpha/2}} 6V_{\text{tet}}\beta u^{3\beta-1-\alpha\beta} |\mathbf{T}^{-1}| dud\rho d\theta
$$

$$
= \iiint \frac{f(u,\bar{\rho},\theta)}{A^\alpha(\theta)} \frac{\bar{\rho}}{(\bar{\rho}^2 + \tilde{d}^2)^{\alpha/2}} 6V_{\text{tet}}\beta u^{3\beta-1-\alpha\beta} r_0^{2-\alpha}\cos^{\alpha-2}\theta |\mathbf{T}^{-1}| dud\bar{\rho} d\theta \qquad (37)
$$

$$
= \iiint \frac{f(u,\tilde{\rho},\theta)}{A^\alpha(\theta)} 6V_{\text{tet}}\beta u^{3\beta-1-\alpha\beta} r_0^{2-\alpha}\cos^{\alpha-2}\theta e^{(2-\alpha)\tilde{\rho}} |\mathbf{T}^{-1}| dud\tilde{\rho} d\theta.
$$

When $\alpha < 2$, the term $\cos^{\alpha-2}$ in Equation (37) reflects the near singularity caused by distorted patch shape during the polar coordinate transformation, and easily to know, we can employ the θ-directional transformation $\theta = \sin^{-1}\tanh\tilde{\theta}$ in Equation (6) with $d\theta = \cos\theta d\tilde{\theta}$ to weaken the near singularity, which is optimal for $\alpha = 1$. As an alternative choice, we can also introduce the improved sigmoidal transformation[37-39] as

$$
\theta = \frac{\pi}{2}(2\sigma - 1), \quad \sigma = \frac{\tilde{\theta}^m}{\tilde{\theta}^m + (1-\tilde{\theta})^m}, \qquad (38)
$$

with $d\theta = \frac{\pi m \tilde{\theta}^{m-1}(1-\tilde{\theta})^{m-1}}{[\tilde{\theta}^m + (1-\tilde{\theta})^m]^2} d\tilde{\theta}$, and correspondingly, Equation (37) can be rewritten as

$$
\iiint \frac{f(x,y,z)}{r^\alpha} dxdydz = \iiint \frac{f(u,\tilde{\rho},\theta)}{A^\alpha(\theta)} 6V_{\text{tet}}\beta u^{3\beta-1-\alpha\beta} r_0^{2-\alpha}\cos^{\alpha-2}\theta e^{(2-\alpha)\tilde{\rho}} |\mathbf{T}^{-1}| dud\tilde{\rho} d\theta
$$

$$
= \iiint \frac{f(u,\tilde{\rho},\tilde{\theta})}{A^\alpha(\tilde{\theta})} 6V_{\text{tet}}\beta u^{3\beta-1-\alpha\beta} r_0^{2-\alpha}\cos^{\alpha-2}\theta e^{(2-\alpha)\tilde{\rho}} \frac{\pi m \tilde{\theta}^{m-1}(1-\tilde{\theta})^{m-1}}{[\tilde{\theta}^m + (1-\tilde{\theta})^m]^2} |\mathbf{T}^{-1}| dud\tilde{\rho} d\tilde{\theta}. \qquad (39)
$$

The effect of the improve sigmoidal transformation is to cluster Gauss points toward $\theta = \pm\frac{\pi}{2}$, and the degree of movement depends on the exponent m. Numerical tests show that the two transformations in θ-direction can get similar results. In this paper, for all the results listed later, the improved sigmoidal transformation with $m = 2$ is used to demonstrate its feasibility.

Example 4.4 (Sensitivity of 3D Duffy-distance transformation to base triangle shape).
To prove the effect of 3D Duffy-distance transformation for tetrahedrons with distorted base shape, tetrahedrons in Example 4.3 are tested for $1/r^\alpha (\alpha = 1$ or $1/2)$, and the relative errors of 3D Duffy-distance transformation with/without the improved sigmoidal transformation are presented in Figures 18 to 20, respectively. Clearly, for distorted base triangles with large aspect ratio, or peak or large obtuse angles at point 3, the 3D Duffy distance transformation can always exert remarkable improvement with higher convergence rate.

5 | EXTENSION TO ARBITRARY SHAPED TETRAHEDRONS

Up to now, the aforementioned 3D Duffy-distance transformation is only suitable for tetrahedrons satisfying the condition of $\mathbf{r}_{12} \perp \Delta 234$. To extend to arbitrary shaped tetrahedrons, subdivision into several subtetrahedrons with the projection point P from singular vertex to base triangle is necessary. Assuming that the projection point is located inside the base triangle, as shown in Figure 21, the original tetrahedral cell is divided into three subcells, ie, 1P23, 1P34, and 1P42. If one of the area of these three base triangles ΔP23, ΔP34, and ΔP42 is smaller than a tolerance, the projection point is located on one edge of base triangle. If two, the projection point lies on one vertex of base triangle. In each case, only subcells with nonzero area of base triangle should be calculated. Especially, when the projection point is located outside of base triangle, if the order of base triangle is clockwise from the opposite view of singular vertex, the corresponding signed volume in Jacobian for this subcell will be negative, hence the superposition rule can be satisfied automatically. Therefore, the subdivision scheme is appropriate for all positions of projection point. In this section, to demonstrate the robustness and efficiency of Duffy-distance transformation, arbitrary shaped tetrahedrons are tested with comparisons to the Duffy transformation, including tetrahedrons with different cell heights and distorted base triangles, as well as various locations of projection point.
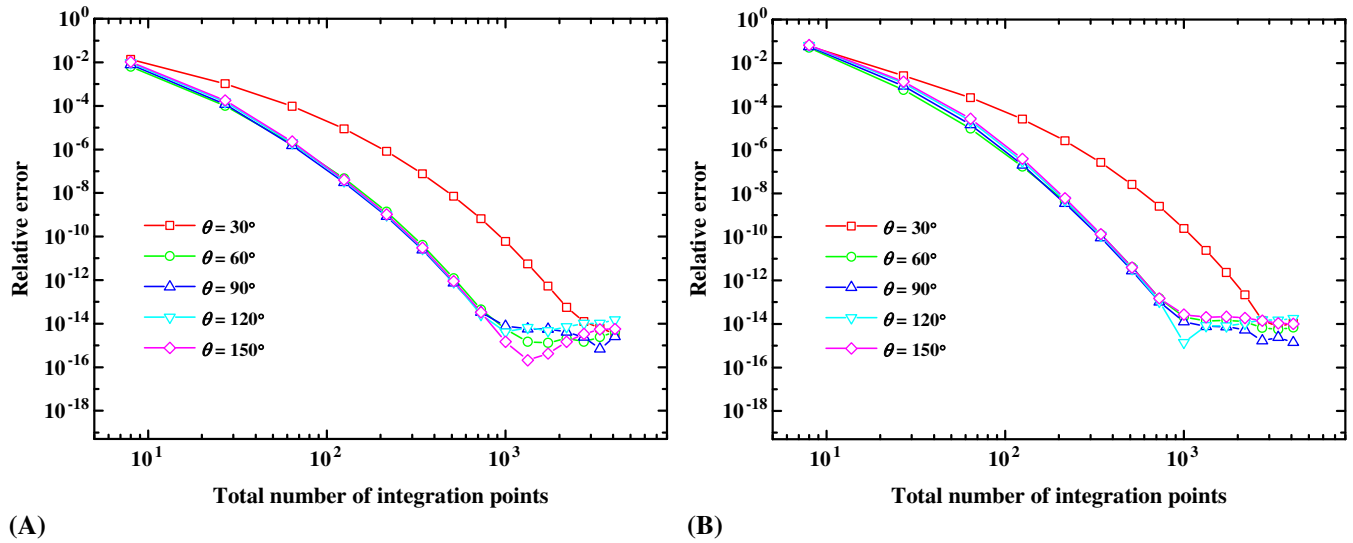
FIGURE 18 Sensitivity of 3D Duffy-distance transformation to inclined angle of base triangle (without the improved sigmoidal transformation). A, $\alpha = 1$; B, $\alpha = 1/2$
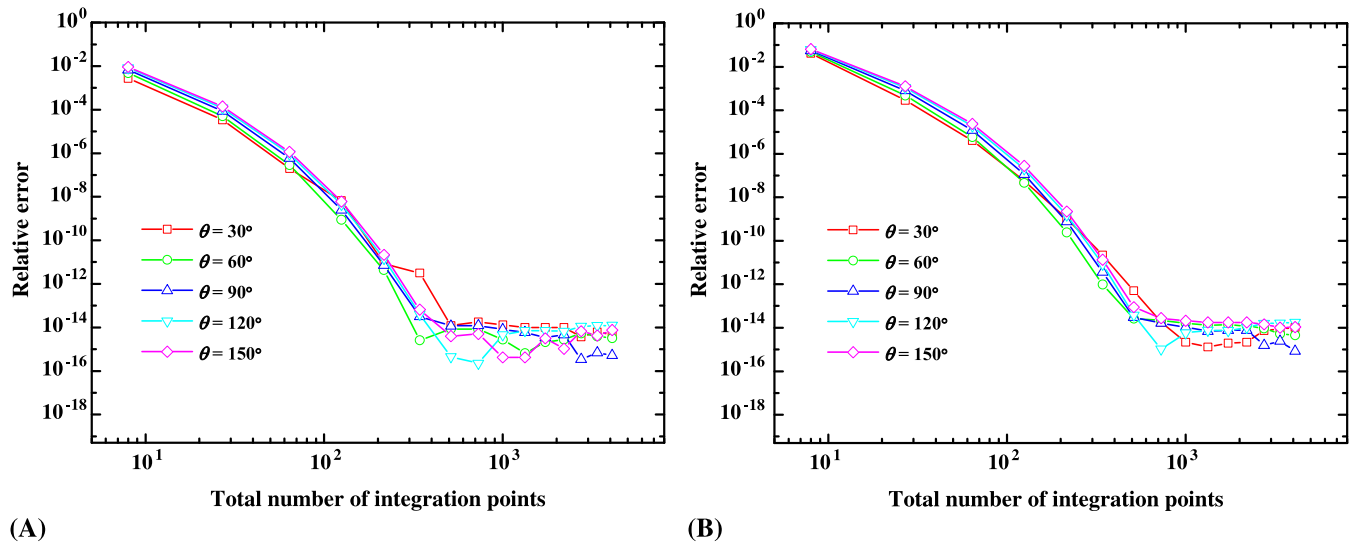

FIGURE 19 Sensitivity of 3D Duffy-distance transformation to inclined angle of base triangle. A, $\alpha = 1$; B, $\alpha = 1/2$

Example 5.1 (Tetrahedrons with different heights).

To verify the sensitivity of 3D Duffy-distance transformation to cell height, tetrahedrons with nodes (0.25, 0.25, h), (0, 0, 0), (0, 1, 0), and (1, 0, 0) are tested for $1/r^\alpha (\alpha = 1$ or $1/2)$ with h taking as 0.5, 0.1, and 0.05, and the projection point is set to be located at (0.25, 0.25, 0). The relative errors for both the Duffy and Duffy-distance transformations are presented in Figure 22. It can be easily observed that, as $h = 0.5$, the Duffy transformation can get slightly better results than the Duffy-distance transformation, whereas, for $h = 0.1$ or 0.05, the Duffy-distance transformation is obviously superior to the Duffy transformation. In contrast to the Duffy transformation, almost the same convergence rate can be achieved with the Duffy-distance transformation for all values of h.

Example 5.2 (Various locations of projection point).

In addition, in order to validate the feasibility to various locations of projection point, tetrahedrons with nodes (a, a, 0.1) (0, 0, 0) (0, 1, 0) and (1, 0, 0) are tested for $1/r^\alpha (\alpha = 1$ or $1/2)$ with a varying along the line from (0, 0, 0.1) to (0.5, 0.5, 0.1), and the cell height is fixed as 0.1. For convenient comparison, 10^3 and 3×7^3 Gauss points are used for the Duffy and Duffy-distance transformations, respectively. The relative errors for various locations of projection point
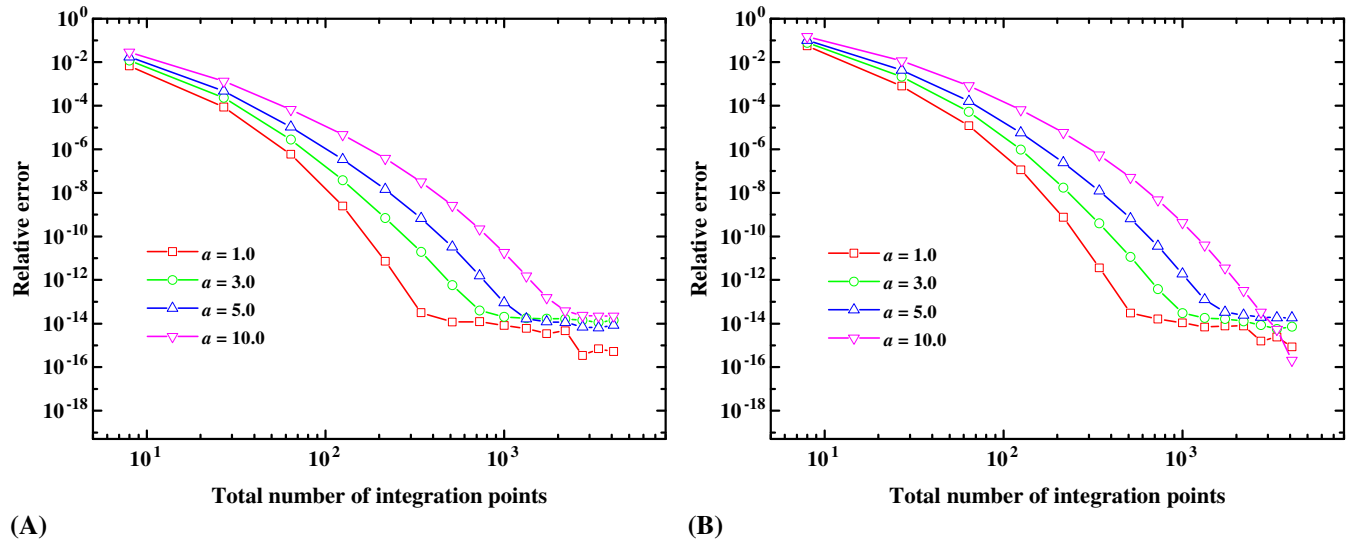
FIGURE 20 Sensitivity of 3D Duffy-distance transformation to aspect ratio of base triangle. A, $\alpha = 1$; B, $\alpha = 1/2$ [Colour figure can be viewed at wileyonlinelibrary.com]
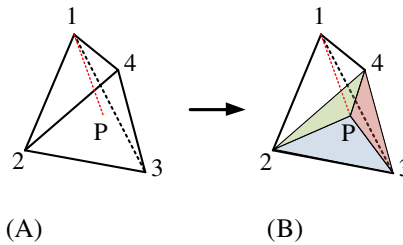

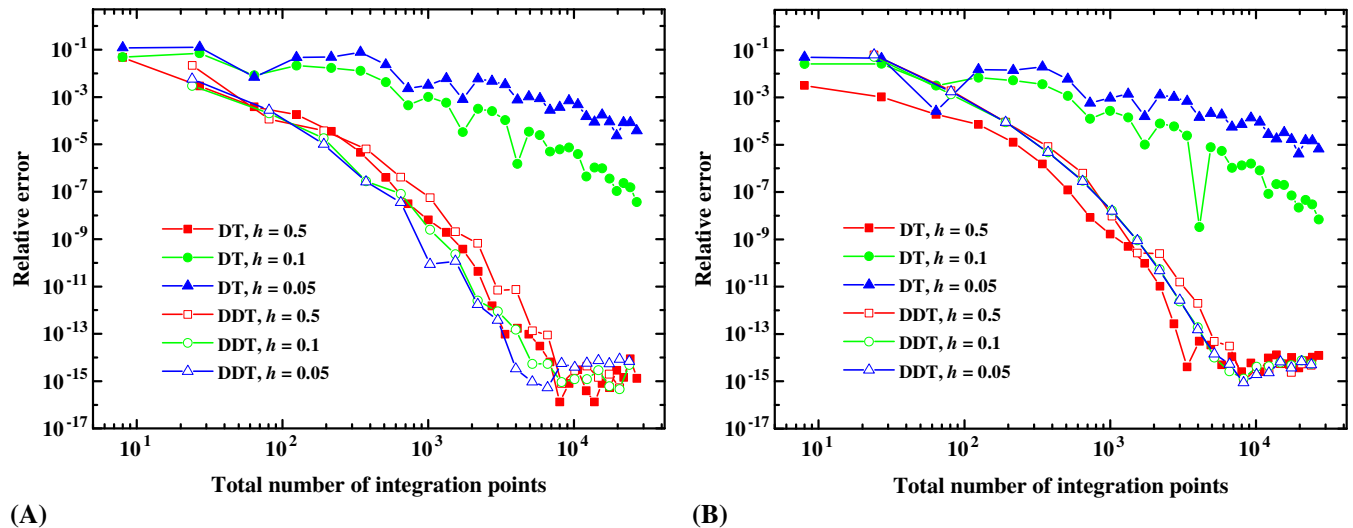**FIGURE 21** Subdivision scheme [Colour figure can be viewed at wileyonlinelibrary.com]

FIGURE 22 Sensitivity to different cell heights. A, $\alpha = 1$; B, $\alpha = 1/2$

are plotted in Figure 23, and the Duffy-distance transformation is apparently superior to the Duffy transformation. The closer the projection point approaches the center of base triangle, the more accurate results can be obtained.

Example 5.3 (Tetrahedrons with distorted base triangle)**.**
To examine the sensitivity of 3D Duffy-distance transformation to distorted base triangle, distorted triangle with nodes $(0, 0, 0)$ $(\cos 120°, \sin 120°, 0)$ and $(1, 0, 0)$ is selected as the base of tetrahedrons with fixed height $h = 0.1$. The projection
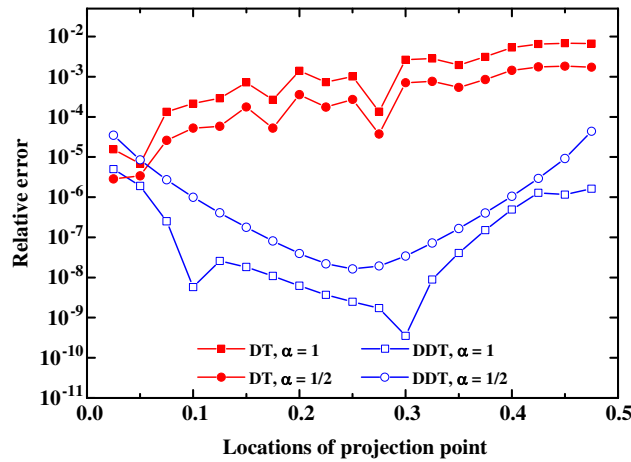
FIGURE 23 Sensitivity to various locations of projection point [Colour figure can be viewed at wileyonlinelibrary.com]
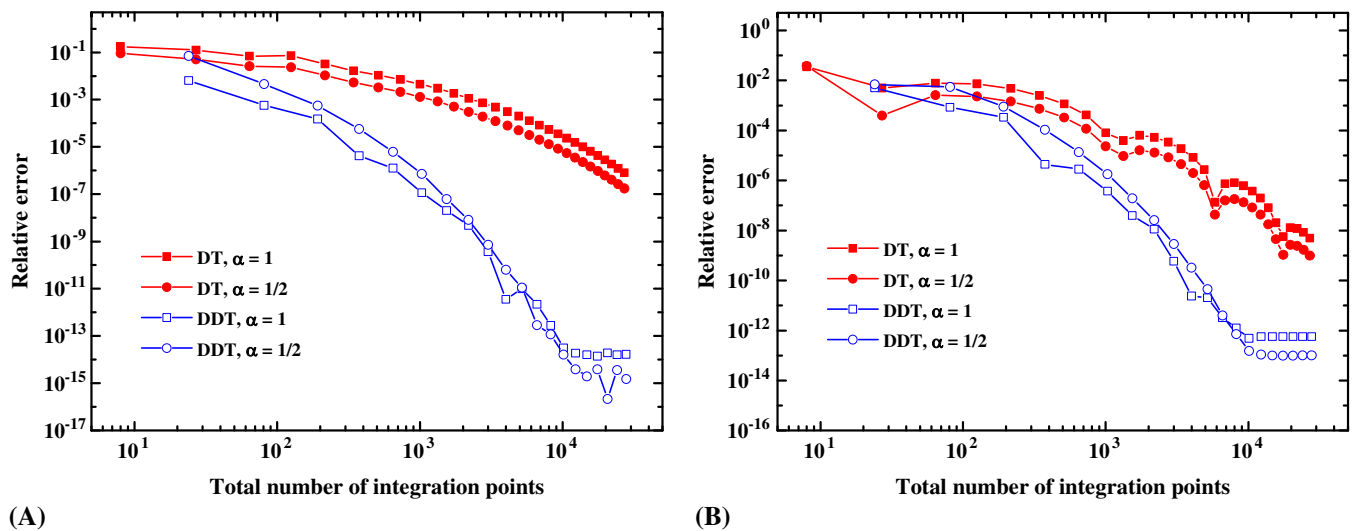

(A)

(B)

FIGURE 24 Convergence curves for tetrahedron with distorted base triangle. A, $\alpha = 1$; B, $\alpha = 1/2$ [Colour figure can be viewed at wileyonlinelibrary.com]

point is set to be located inside or outside of the base triangle, ie, $\mathbf{x}^{(P)} = (0.15, 0.25, 0)$ or $\mathbf{x}^{(P)} = (0.5, 0.5, 0)$, respectively. The relative errors for $1/r^{\alpha}(\alpha = 1$ or $1/2)$ are given in Figure 24. As it can be seen, the Duffy-distance transformation can always get more accurate results with higher convergence rate regardless of the distorted base shape.

6 | 3D CONFORMAL PRECONDITIONING STRATEGY

Numerical integrations over tetrahedral elements with singular point inside are often encountered in the GFEM/XFEM. These tetrahedral elements are firstly divided into three tetrahedral cells in local space-$\xi\eta\zeta$ with the singular point being one vertex, and then the proposed Duffy-distance transformation can be utilized for each tetrahedral cell. However, numerical tests on arbitrary shaped tetrahedral elements show that the desired precision as the Duffy-distance transformation cannot be obtained unless the tetrahedral elements is similar to the standard unit tetrahedron with nodes $(0, 0, 0)$, $(1, 0, 0)$, $(0, 1, 0)$ and $(0, 0, 1)$, and the accuracy varies depending heavily on the distortion of element shape. Therefore, we infer that the iso-parametric transformation from global space-xyz to local space-$\xi\eta\zeta$ may bring another near singularity owing to the distorted element shape, which will be discovered theoretically in this section.

Considering an arbitrary tetrahedral element with singular point inside, the tetrahedral element is firstly mapped into the standard unit tetrahedron with the iso-parametric transformation (Figure 25A-B), and then a local spherical
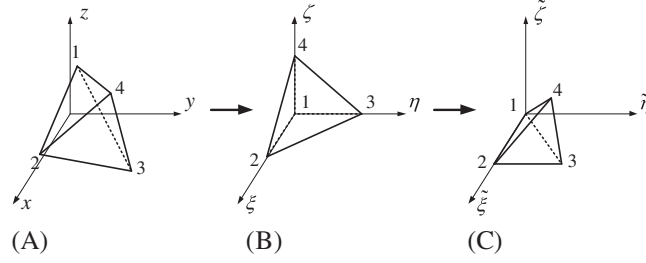
FIGURE 25 3D conformal preconditioning strategy

coordinate system centered at the singular point $\mathbf{x}^{(S)}$ can be established via

$$
\begin{cases}
\xi = \xi^{(S)} + \rho \sin \phi \cos \theta \\
\eta = \eta^{(S)} + \rho \sin \phi \sin \theta \\
\zeta = \zeta^{(S)} + \rho \cos \phi.
\end{cases}
\tag{40}
$$

The following relations can be obtained via the Taylor expansion:

$$
\begin{aligned}
x_k - x_k^{(S)} &= \frac{\partial x_k}{\partial \xi}\bigg|_{\mathbf{x}=\mathbf{x}^{(S)}} \left(\xi - \xi^{(S)}\right) + \frac{\partial x_k}{\partial \eta}\bigg|_{\mathbf{x}=\mathbf{x}^{(S)}} \left(\eta - \eta^{(S)}\right) + \frac{\partial x_k}{\partial \zeta}\bigg|_{\mathbf{x}=\mathbf{x}^{(S)}} \left(\zeta - \zeta^{(S)}\right) \\
&= \rho \left(\frac{\partial x_k}{\partial \xi}\bigg|_{\mathbf{x}=\mathbf{x}^{(S)}} \sin \phi \cos \theta + \frac{\partial x_k}{\partial \eta}\bigg|_{\mathbf{x}=\mathbf{x}^{(S)}} \sin \phi \sin \theta + \frac{\partial x_k}{\partial \zeta}\bigg|_{\mathbf{x}=\mathbf{x}^{(S)}} \cos \phi \right) \\
&= \rho A_k (\phi, \theta)
\end{aligned}
\tag{41}
$$

with

$$
A_k (\phi, \theta) = \frac{\partial x_k}{\partial \xi}\bigg|_{\mathbf{x}=\mathbf{x}^{(S)}} \sin \phi \cos \theta + \frac{\partial x_k}{\partial \eta}\bigg|_{\mathbf{x}=\mathbf{x}^{(S)}} \sin \phi \sin \theta + \frac{\partial x_k}{\partial \zeta}\bigg|_{\mathbf{x}=\mathbf{x}^{(S)}} \cos \phi.
\tag{42}
$$

Then, the square distance from arbitrary point to the singular point can be written as

$$
r^2 = \sum_{k=1}^{3} \left(x_k - x_k^{(S)} \right)^2 = \rho^2 A^2 (\phi, \theta)
\tag{43}
$$

with

$$
A (\phi, \theta) = \left\{ \sum_{k=1}^{3} A_k^2 (\phi, \theta) \right\}^{1/2}.
\tag{44}
$$

Note that $A(\phi, \theta)$ is directly related to the shape of tetrahedral elements, we assume $\mathbf{u}_1$, $\mathbf{u}_2$, and $\mathbf{u}_3$ being the three line vectors of Jacobian matrix at singular point $\mathbf{x}^{(S)}$, ie,

$$
\mathbf{u}_1 = \left[\frac{\partial x}{\partial \xi}\bigg|_{\mathbf{x}=\mathbf{x}^{(S)}}, \frac{\partial y}{\partial \xi}\bigg|_{\mathbf{x}=\mathbf{x}^{(S)}}, \frac{\partial z}{\partial \xi}\bigg|_{\mathbf{x}=\mathbf{x}^{(S)}} \right] = [x_2 - x_1, y_2 - y_1, z_2 - z_1] = \mathbf{r}_{12}
\tag{45}
$$

$$
\mathbf{u}_2 = \left[\frac{\partial x}{\partial \eta}\bigg|_{\mathbf{x}=\mathbf{x}^{(S)}}, \frac{\partial y}{\partial \eta}\bigg|_{\mathbf{x}=\mathbf{x}^{(S)}}, \frac{\partial z}{\partial \eta}\bigg|_{\mathbf{x}=\mathbf{x}^{(S)}} \right] = [x_3 - x_1, y_3 - y_1, z_3 - z_1] = \mathbf{r}_{13}
\tag{46}
$$

$$
\mathbf{u}_3 = \left[\frac{\partial x}{\partial \zeta}\bigg|_{\mathbf{x}=\mathbf{x}^{(S)}}, \frac{\partial y}{\partial \zeta}\bigg|_{\mathbf{x}=\mathbf{x}^{(S)}}, \frac{\partial z}{\partial \zeta}\bigg|_{\mathbf{x}=\mathbf{x}^{(S)}} \right] = [x_4 - x_1, y_4 - y_1, z_4 - z_1] = \mathbf{r}_{14}.
\tag{47}
$$

Then, $A(\phi, \theta)$ can be rewritten as

$$
\begin{aligned}
A (\phi, \theta) &= \sqrt{ \sum_{k=1}^{3} \left(\frac{\partial x_k}{\partial \xi}\bigg|_{\mathbf{x}=\mathbf{x}^{(S)}} \sin \phi \cos \theta + \frac{\partial x_k}{\partial \eta}\bigg|_{\mathbf{x}=\mathbf{x}^{(S)}} \sin \phi \sin \theta + \frac{\partial x_k}{\partial \zeta}\bigg|_{\mathbf{x}=\mathbf{x}^{(S)}} \cos \phi \right)^2 } \\
&= \sqrt{ \begin{aligned} &\mathbf{u}_1^2 \sin^2 \phi \cos^2 \theta + \mathbf{u}_2^2 \sin^2 \phi \sin^2 \theta + \mathbf{u}_3^2 \cos^2 \phi \\ &+ \mathbf{u}_1 \cdot \mathbf{u}_2 \sin^2 \phi \cos 2\theta + \mathbf{u}_1 \cdot \mathbf{u}_3 \sin 2\phi \cos \theta + \mathbf{u}_2 \cdot \mathbf{u}_3 \sin 2\phi \sin \theta \end{aligned} }.
\end{aligned}
\tag{48}
$$

Similar to the 2D case in Section 4.3, in order to get a constant $A(\phi, \theta)$, the following conditions

$$\begin{cases} |\mathbf{u}_1| = |\mathbf{u}_2| = |\mathbf{u}_3| \\ \mathbf{u}_1 \bullet \mathbf{u}_2 = \mathbf{u}_1 \bullet \mathbf{u}_3 = \mathbf{u}_2 \bullet \mathbf{u}_3 = 0 \end{cases} \tag{49}$$

should be satisfied, resulting in $A(\phi, \theta) = |\mathbf{u}_1| = |\mathbf{u}_2| = |\mathbf{u}_3|$, and the corresponding 3D conformal preconditioning strategy from space-$\xi\eta\zeta$ to space-$\tilde{\xi}\tilde{\eta}\tilde{\zeta}$ (Figure 25B-C) can be constructed by the inverse interpolation

$$\tilde{\mathbf{x}} = \sum_{i=1}^{4} \phi_i(v, w)\, \tilde{\mathbf{x}}^{(i)} \tag{50}$$

with

$$\phi_1 = 1 - \xi - \eta - \zeta, \quad \phi_2 = \xi, \quad \phi_3 = \eta, \quad \phi_4 = \zeta, \tag{51}$$

where $\tilde{\mathbf{x}}^{(i)}$ is the node coordinates of new tetrahedron. Substituting Equation (51) into Equation (50) yields

$$\begin{bmatrix} \tilde{\xi} \\ \tilde{\eta} \\ \tilde{\zeta} \end{bmatrix} = \mathbf{T} \begin{bmatrix} 1 \\ \xi \\ \eta \\ \zeta \end{bmatrix}, \quad \mathbf{T} = \begin{bmatrix} \tilde{\xi}^{(1)} & \tilde{\xi}^{(2)} - \tilde{\xi}^{(1)} & \tilde{\xi}^{(3)} - \tilde{\xi}^{(1)} & \tilde{\xi}^{(4)} - \tilde{\xi}^{(1)} \\ \tilde{\eta}^{(1)} & \tilde{\eta}^{(2)} - \tilde{\eta}^{(1)} & \tilde{\eta}^{(3)} - \tilde{\eta}^{(1)} & \tilde{\eta}^{(4)} - \tilde{\eta}^{(1)} \\ \tilde{\zeta}^{(1)} & \tilde{\zeta}^{(2)} - \tilde{\zeta}^{(1)} & \tilde{\zeta}^{(3)} - \tilde{\zeta}^{(1)} & \tilde{\zeta}^{(4)} - \tilde{\zeta}^{(1)} \end{bmatrix}. \tag{52}$$

To obtain a linear mapping, $\left(\tilde{\xi}^{(1)}, \tilde{\eta}^{(1)}, \tilde{\zeta}^{(1)}\right)$ is set to be $(0, 0, 0)$. In addition, we assume node 2 and 3 are in the same place of $\tilde{\zeta} = 0$, and $\left(\tilde{\xi}^{(2)}, \tilde{\eta}^{(2)}, \tilde{\zeta}^{(2)}\right) = (1, 0, 0)$. Consequently, node 4 should be $\left(0, 0, \tilde{\zeta}^{(4)}\right)$ because $\mathbf{u}_1 \cdot \mathbf{u}_3 = \mathbf{u}_2 \cdot \mathbf{u}_3 = 0$, and the transformation matrix $\mathbf{T}$ will degenerate as

$$\begin{bmatrix} \tilde{\xi} \\ \tilde{\eta} \\ \tilde{\zeta} \end{bmatrix} = \mathbf{T} \begin{bmatrix} \xi \\ \eta \\ \zeta \end{bmatrix}, \quad \mathbf{T} = \begin{bmatrix} 1 & \tilde{\xi}^{(3)} & 0 \\ 0 & \tilde{\eta}^{(3)} & 0 \\ 0 & 0 & \tilde{\zeta}^{(4)} \end{bmatrix}, \quad \mathbf{T}^{-1} = \frac{1}{|\mathbf{T}|} \begin{bmatrix} \tilde{\eta}^{(3)}\tilde{\zeta}^{(4)} & -\tilde{\xi}^{(3)}\tilde{\zeta}^{(4)} & 0 \\ 0 & \tilde{\zeta}^{(4)} & 0 \\ 0 & 0 & \tilde{\eta}^{(3)} \end{bmatrix}. \tag{53}$$

The three line vectors of Jacobian matrix at singular point $\mathbf{x}^{(S)}$ in Equations (45)-(47) will be further transformed as

$$(\tilde{\mathbf{u}}_1, \tilde{\mathbf{u}}_2, \tilde{\mathbf{u}}_3) = (\mathbf{u}_1, \mathbf{u}_2, \mathbf{u}_3)\, \mathbf{T}^{-1} = \frac{1}{|\mathbf{T}|} \left[\tilde{\eta}^{(3)}\tilde{\zeta}^{(4)}\mathbf{u}_1, -\tilde{\xi}^{(3)}\tilde{\zeta}^{(4)}\mathbf{u}_1 + \tilde{\zeta}^{(4)}\mathbf{u}_2, \tilde{\eta}^{(3)}\mathbf{u}_3 \right]. \tag{54}$$

Solving the remaining conditions in Equation (49), ie, $|\tilde{\mathbf{u}}_1| = |\tilde{\mathbf{u}}_2| = |\tilde{\mathbf{u}}_3|$ and $\tilde{\mathbf{u}}_1 \cdot \tilde{\mathbf{u}}_2 = 0$, we have

$$\begin{cases} \tilde{\xi}^{(3)} = \frac{\cos\gamma_{12}}{\lambda_{12}} \\ \tilde{\eta}^{(3)} = \pm\frac{\sin\gamma_{12}}{\lambda_{12}} \\ \tilde{\zeta}^{(4)} = \pm\frac{1}{\lambda_{13}} \end{cases} \Rightarrow \begin{cases} \tilde{\xi}^{(3)} = \frac{\cos\gamma_{12}}{\lambda_{12}} \\ \tilde{\eta}^{(3)} = \frac{\sin\gamma_{12}}{\lambda_{12}} \\ \tilde{\zeta}^{(4)} = \frac{1}{\lambda_{13}} \end{cases} \text{or} \begin{cases} \tilde{\xi}^{(3)} = \frac{\cos\gamma_{12}}{\lambda_{12}} \\ \tilde{\eta}^{(3)} = -\frac{\sin\gamma_{12}}{\lambda_{12}} \\ \tilde{\zeta}^{(4)} = -\frac{1}{\lambda_{13}} \end{cases} \tag{55}$$

with

$$\lambda_{12} = \frac{|\mathbf{u}_1|}{|\mathbf{u}_2|}, \quad \lambda_{13} = \frac{|\mathbf{u}_1|}{|\mathbf{u}_3|}, \quad \cos\gamma_{12} = \frac{\mathbf{u}_1 \cdot \mathbf{u}_2}{|\mathbf{u}_1||\mathbf{u}_2|}. \tag{56}$$

Finally, two groups of solution in Equation (55) can be determined by introducing the node order condition. For the first case, the final transformation matrix $\mathbf{T}$ can be written as

$$\mathbf{T} = \begin{bmatrix} 1 & \frac{\cos\gamma_{12}}{\lambda_{12}} & 0 \\ 0 & \frac{\sin\gamma_{12}}{\lambda_{12}} & 0 \\ 0 & 0 & \frac{1}{\lambda_{13}} \end{bmatrix}, \quad \mathbf{T}^{-1} = \begin{bmatrix} 1 & -\frac{\cos\gamma_{12}}{\sin\gamma_{12}} & 0 \\ 0 & \frac{\lambda_{12}}{\sin\gamma_{12}} & 0 \\ 0 & 0 & \lambda_{13} \end{bmatrix}. \tag{57}$$

Example 6.1 (Tetrahedral element with distorted shape).

To prove the effect of 3D conformal preconditioning strategy, a distorted tetrahedral element with nodes $(0, 0, 0)$, $(\cos120°, \sin120°, 0)$, $(1, 0, 0)$, and $(0,0,5)$ are tested with $\alpha = 1$ or $1/2$, and the singular point is assigned at $(\xi^{(S)}, \eta^{(S)}, \zeta^{(S)}) = (0.3, 0.3, 0.3)$, which is close to the center of $\triangle 234$. The relative errors for the 3D Duffy-distance transformation with/without conformal preconditioning strategy are presented in Figure 26. We can conclude that, with the increase of evaluation points, the 3D Duffy-distance transformation with conformal preconditioning strategy can
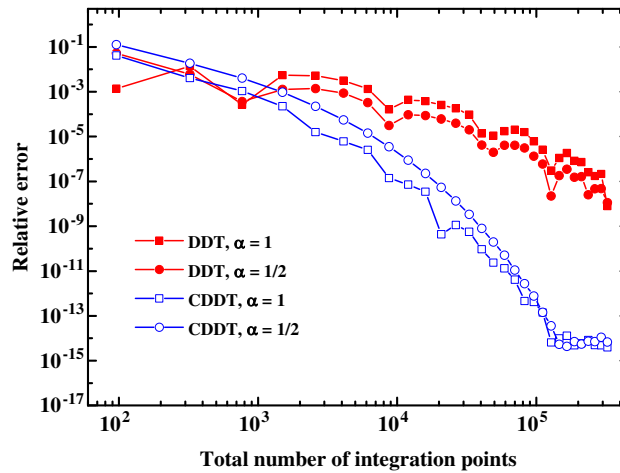
FIGURE 26 Convergence curves for tetrahedron element with distorted shape [Colour figure can be viewed at wileyonlinelibrary.com]
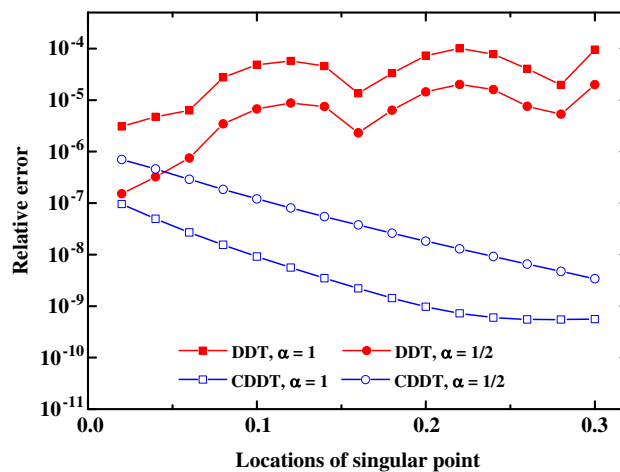

FIGURE 27 Sensitivity to various locations of singular point [Colour figure can be viewed at wileyonlinelibrary.com]

get more accurate results with higher convergence rate compared to those without conformal preconditioning strategy. Therefore, the 3D conformal preconditioning strategy can enable the 3D Duffy-distance transformation to be applicable for arbitrary shaped tetrahedral elements.

Example 6.2. (Various locations of singular point).

In addition, we also investigate the sensitivity to various locations of singular point. The same tetrahedral element in 6.1 is adopted with singular point $(\xi^{(S)}, \eta^{(S)}, \zeta^{(S)})$ moving along the line from $(0, 0, 0)$ to $(1/3, 1/3, 1/3)$, and $4 \times 3 \times 14^3$ Gauss points are used, where 4 and 3 represent the total number of tetrahedral cells and subcells, respectively. The relative errors for the 3D Duffy-distance transformation with/without conformal preconditioning strategy are given in Figure 27. Without any doubt, the 3D Duffy-distance transformation with conformal preconditioning strategy is an optimal choice, and the closer the singular point approaches the center of $\Delta 234$, the more accurate results can be obtained.

7 | SUMMARIES

In this paper, the near singularities caused by distorted integral patch/cell shape during the implementation of generalized Duffy transformation are discovered numerically and theoretically. In order to damp out the near singularities, the Duffy-distance transformation is developed for the 2D and 3D vertex singularities. Meanwhile, the 3D conformal preconditioning strategy is constructed to eliminate the near singularity caused by element shape distortion during the iso-parametric transformation, which enables the Duffy-distance transformation to be applicable for arbitrary shaped

tetrahedral elements. Numerous numerical examples for arbitrary shaped triangles and tetrahedrons are presented to demonstrate its robustness and efficiency, along with comparisons to the generalized Duffy transformation.

For the 2D case, the near singularities are caused by the distorted integral patch shape, and the distance transformation in v-direction is introduced to damp out the singularity. Numerical results show that, for integrals of type $O(1/r)$, 2×2 Gauss points are enough to achieve the machine precision, whereas, for $\alpha \neq 1$, remarkable improvement can be observed. As a byproduct, the so-called parabolic transformation is generalized into the Duffy-sinh transformation, which is equivalent to the proposed Duffy-distance transformation.

For the 3D case, the near singularities derive from both the cell height and the base triangle shape. The arbitrary shaped tetrahedral cell is firstly subdivided into several subcells with the projection point from singular vertex to base triangle. Then, after transformation into a triangular prism for each subcell, the 2D conformal preconditioning strategy is employed to eliminate the near singularity caused by distorted base triangle shape. Finally, a local coordinate polar coordinate system is established with the origin located at the projection point, and the distance transformation in radial direction and the sigmoidal transformation in angular direction are utilized jointly to damp out the near singularities. Numerical results demonstrate that the Duffy-distance transformation is always superior to the Duffy transformation with higher convergence rate.

When applying the Duffy-distance transformation into tetrahedral elements with singular point inside, the iso-parametric transformation brings another near singularity caused by element shape distortion, and the 3D conformal preconditioning strategy is constructed to eliminate the near singularity. The corresponding 2D conformal preconditioning strategy has also been developed for triangular and quadrilateral elements, and interested readers can refer to the work of Lv et al.[40] The proposed scheme can be extended to other orders of singularity in straightforward fashion. Configurations for edge case as in the work of Minnebo[30] and further applications in the GFEM/XFEM framework will be the sequential work.

ORCID

Jia-He Lv https://orcid.org/0000-0002-4175-5210
Timon Rabczuk https://orcid.org/0000-0002-7150-296X

REFERENCES

1. Strouboulis T, Copps K, Babuška I. The generalized finite element method: an example of its implementation and illustration of its performance. *Int J Numer Methods Eng*. 2000;47(8):1401-1417.

2. Duarte CA, Babuška I, Oden JT. Generalized finite element methods for three-dimensional structural mechanics problems. *Comput Struct*. 2000;77(2):215-232.

3. Belytschko T, Black T. Elastic crack growth in finite elements with minimal remeshing. *Int J Numer Methods Eng*. 1999;45(5):601-620.

4. Moës N, Dolbow J, Belytschko T. A finite element method for crack growth without remeshing. *Int J Numer Methods Eng*. 1999;46(1):131-150.

5. Sukumar N, Moës N, Moran B, Belytschko T. Extended finite element method for three-dimensional crack modelling. *Int J Numer Methods Eng*. 2000;48(11):1549-1570.

6. Zheng H, Xu DD. New strategies for some issues of numerical manifold method in simulation of crack propagation. *Int J Numer Methods Eng*. 2014;97(13):986-1010.

7. Zheng H, Liu F, Du XL. Complementarity problem arising from static growth of multiple cracks and MLS-based numerical manifold method. *Comput Methods Appl Mech Eng*. 2015;295:150-171.

8. Yang YT, Tang XH, Zheng H, Liu Q, Liu Z. Hydraulic fracturing modeling using the enriched numerical manifold method. *App Math Model*. 2018;53:462-486.

9. Yang YT, Tang XH, Zheng H, Liu Q, He L. Three-dimensional fracture propagation with numerical manifold method. *Eng Anal Bound Elem*. 2016;72:65-77.

10. Melenk JM, Babuška I. The partition of unity finite element method: basic theory and applications. *Comput Methods Appl Mech Eng*. 1996;139(1-4):289-314.

11. Elguedj T, Gravouil A, Combescure A. Appropriate extended functions for X-FEM simulation of plastic fracture mechanics. *Comput Methods Appl Mech Eng*. 2006;195(7):501-515.

12. Lecampion B. An extended finite element method for hydraulic fracture problems. *Int J Numer Methods Biomed Eng*. 2009;25(2):121-133.

13. Waisman H, Belytschko T. Parametric enrichment adaptivity by the extended finite element method. *Int J Numer Methods Eng*. 2008;73(12):1671-1692.

14. Strouboulis T, Babuška I, Copps K. The design and analysis of the generalized finite element method. *Comput Methods Appl Mech Eng*. 2000;181(1-3):43-69.

15. Xiao QZ, Karihaloo BL. Improving the accuracy of XFEM crack tip fields using higher order quadrature and statically admissible stress recovery. *Int J Numer Methods Eng*. 2006;66(9):1378-1410.

16. Schweitzer MA. An adaptive hp-version of the multilevel particle–partition of unity method. *Comput Methods Appl Mech Eng*. 2009;198(13-14):1260-1272.

17. Natarajan S, Mahapatra DR, Bordas S. Integrating strong and weak discontinuities without integration subcells and example applications in an XFEM/GFEM framework. *Int J Numer Methods Eng*. 2010;83(3):269-294.

18. Ventura G. On the elimination of quadrature subcells for discontinuous functions in the eXtended finite-element method. *Int J Numer Methods Eng*. 2006;66(5):761-795.

19. Chin EB, Lasserre JB, Sukumar N. Modeling crack discontinuities without element-partitioning in the extended finite element method. *Int J Numer Methods Eng*. 2017;110(11):1021-1048.

20. Duffy MG. Quadrature over a pyramid or cube of integrands with a singularity at a vertex. *SIAM J Numer Anal*. 1982;19(6):1260-1262.

21. Laborde P, Pommier J, Renard Y, Salaün M. High-order extended finite element method for cracked domains. *Int J Numer Methods Eng*. 2005;64(3):354-381.

22. Mousavi SE, Sukumar N. Generalized Duffy transformation for integrating vertex singularities. *Computational Mechanics*. 2010;45(2):127-140.

23. Mousavi SE, Sukumar N. Generalized Gaussian quadrature rules for discontinuities and crack singularities in the extended finite element method. *Comput Methods Appl Mech Eng*. 2010;199(49):3237-3249.

24. Cano A, Moreno C. A new method for numerical integration of singular functions on the plane. *Numerical Algorithms*. 2015;68(3):547-568.

25. Cao-Rial MT, Moreno C, Quintela P. A new methodology for element partition and integration procedures for XFEM. *Finite Elem Anal Des*. 2016;113:1-13.

26. Cano A, Moreno C. Transformation methods for the numerical integration of three-dimensional singular functions. *J Sci Comput*. 2017;71(2):571-593.

27. Béchet É, Minnebo H, Moës N, Burgardt B. Improved implementation and robustness study of the X-FEM for stress analysis around cracks. *Int J Numer Methods Eng*. 2005;64(8):1033-1056.

28. Park K, Pereira JP, Duarte CA, Paulino GH. Integration of singular enrichment functions in the generalized/extended finite element method for three-dimensional problems. *Int J Numer Methods Eng*. 2009;78(10):1220-1257.

29. Nagarajan A, Mukherjee S. A mapping method for numerical evaluation of two-dimensional integrals with $1/r$ singularity. *Computational Mechanics*. 1993;12(1):19-26.

30. Minnebo H. Three-dimensional integration strategies of singular functions introduced by the XFEM in the LEFM. *Int J Numer Methods Eng*. 2012;92(13):1117-1138.

31. Sukumar N, Dolbow JE, Moës N. Extended finite element method in computational fracture mechanics: a retrospective examination. *Int J Fract*. 2015;196(1-2):189-206.

32. Hayami K. Variable transformations for nearly singular integrals in the boundary element method. *Publ Res Inst Math Sci*. 2005;41(4):821-842.

33. Ma H, Kamiya N. Distance transformation for the numerical evaluation of near singular boundary integrals with various kernels in boundary element method. *Eng Anal Bound Elem*. 2002;26(4):329-339.

34. Ma H, Kamiya N. A general algorithm for the numerical evaluation of nearly singular boundary integrals of various orders for two- and three-dimensional elasticity. *Computational Mechanics*. 2002;29(4):277-288.

35. Johnston PR, Elliott D. A sinh transformation for evaluating nearly singular boundary element integrals. *Int J Numer Methods Eng*. 2005;62(4):564-578.

36. Lv JH, Miao Y, Zhu HP. The distance sinh transformation for the numerical evaluation of nearly singular integrals over curved surface elements. *Computational Mechanics*. 2014;53(2):359-367.

37. Johnston PR. Application of sigmoidal transformations to weakly singular and near-singular boundary element integrals. *Int J Numer Methods Eng*. 1999;45(10):1333-1348.

38. Rong JJ, Wen LH, Xiao JY. Efficiency improvement of the polar coordinate transformation for evaluating BEM singular integrals on curved elements. *Eng Anal Bound Elem*. 2014;38:83-93.

39. Lv JH, Feng XT, Yan F, Jiang Q. Efficient evaluation of integrals with kernel $1/r^\chi$ for quadrilateral elements with irregular shape. *Eng Anal Bound Elem*. 2015;61:33-41.

40. Lv JH, Jiao YY, Wriggers P, Rabczuk T, Feng XT, Tan F. Efficient integration of crack singularities in the extended finite element method: Duffy-distance transformation and conformal preconditioning strategy. *Comput Methods Appl Mech Eng*. 2018;340:559-576.